EUROPEAN ORGANISATION FOR NUCLEAR RESEARCH (CERN)

Submitted to: EPJC

CERN-EP-2022-267
2nd March 2023

Search for pair production of third-generation leptoquarks decaying into a bottom quark and a τ-lepton with the ATLAS detector

The ATLAS Collaboration

A search for pair-produced scalar or vector leptoquarks decaying into a b-quark and a τ-lepton is presented using the full LHC Run 2 (2015–2018) data sample of 139 fb^{-1} collected with the ATLAS detector in proton–proton collisions at a centre-of-mass energy of $\sqrt{s} = 13$ TeV. Events in which at least one τ-lepton decays hadronically are considered, and multivariate discriminants are used to extract the signals. No significant deviations from the Standard Model expectation are observed and 95% confidence-level upper limits on the production cross-section are derived as a function of leptoquark mass and branching ratio into the τ-lepton. For scalar leptoquarks, masses below 1490 GeV are excluded assuming a 100% branching ratio, while for vector leptoquarks the corresponding limit is 1690 GeV (1960 GeV) in the minimal-coupling (Yang–Mills) scenario.

1 Introduction

Many extensions of the Standard Model (SM) of particle physics predict particles known as leptoquarks (LQs) [1–7]. These particles provide a connection between the lepton and quark sectors, which are similar in structure in the SM. LQs can be scalar (spin-0) or vector (spin-1) bosons, and they carry colour and a fractional electric charge. They also have non-zero lepton and baryon numbers, and decay into quark–lepton pairs. They can mediate neutral currents, and therefore can potentially provide an explanation for hints of violations of lepton universality observed in flavour experiments [8–14].

LQs could be produced singly or in pairs in proton–proton (pp) collisions at the LHC, and this analysis targets pair-produced LQs that couple strongly to the third generation of quarks and leptons. Within the Buchmüller–Rückl–Wyler (BRW) model [15], which is the benchmark for scalar LQs in this analysis, it is assumed that these LQs can only interact within the same family via a Yukawa interaction. This interaction is described by two parameters, a model parameter β and a coupling parameter λ. In the benchmark models considered in this paper, the pair-production cross-section is independent of λ. This analysis also considers pair-production of vector LQs [16] corresponding to the U_1 state in the BRW classification [15]. The scenarios considered in this model differ by a dimensionless coupling constant k, which is zero for the minimal-coupling scenario and one for the Yang–Mills scenario. For both scalar and vector LQs, the parameter β controls the decay into charged leptons. For these third generation LQs, results are generally given in terms of the branching ratio ($\mathcal{B}$) and mass of the LQ (m_{LQ}).

ATLAS and CMS have published searches for LQs coupling to the first, second and third generations [17–26]. Each generation of LQs is split into up-type and down-type LQs with different electric charges. For instance, for the third generation they are split into up-type LQs ($\mathrm{LQ}_3^{\mathrm{u}}$), which decay into $b\tau$ or $t\nu$, and down-type LQs ($\mathrm{LQ}_3^{\mathrm{d}}$), which decay into $t\tau$ or $b\nu$. Both types of LQs are currently excluded for masses below 1150 GeV for the BRW model, for all values of $\mathcal{B}$.

This paper updates the ATLAS search for an up-type LQ pair decaying into $b\tau$ [18], shown in Figure 1, using the full Run 2 data sample and an updated analysis strategy, prioritising high LQ masses that are not yet excluded for the benchmark models considered. Analysis improvements include updated analysis-optimisation and background-estimation methods, as well as updates to several object identification algorithms. The analysis signature is two jets, at least one of which must be identified as containing a b-hadron, and two τ-leptons. For the τ-leptons, the cases considered are where both decay hadronically or where one τ-lepton decays into a light lepton (electron or muon, ℓ) and neutrinos and the other decays hadronically. The mass range considered for the LQ is from 300 GeV to 2000 GeV. The extraction of the signals is performed through a simultaneous likelihood fit to multivariate discriminants. For the results, both scalar and vector LQs are considered, with the limits on vector LQs interpreted in the context of two scenarios, the Yang–Mills scenario and the minimal-coupling scenario [27].

The paper is structured as follows. After a brief description of the ATLAS detector, the data sample, simulated backgrounds and simulated signals are described. This is followed by a description of the event reconstruction, the object selection, the event selections for the signal regions, and the multivariate discriminants that are used in the final fit. The next sections include a description of the data-driven background estimation methods, the systematic uncertainties, and finally the statistical methods and results.

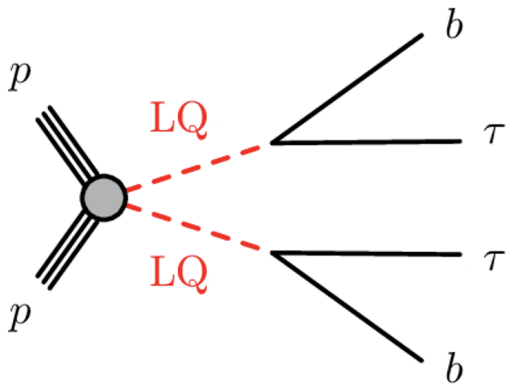

Figure 1: Pair production of a leptoquark (LQ) and its subsequent decay into a b-quark and a τ-lepton.

2 ATLAS detector

The ATLAS detector [28] at the LHC is a multipurpose particle detector with a forward–backward symmetric cylindrical geometry and a near 4π coverage in solid angle.[1] The inner tracking detector consists of pixel and microstrip silicon detectors covering the pseudorapidity region $|\eta| < 2.5$, surrounded by a transition radiation tracker to enhance electron identification in the range of $|\eta| < 2.0$. An additional innermost pixel layer, the insertable B-layer [29, 30], was added before Run 2 of the LHC. The inner detector (ID) is surrounded by a thin superconducting solenoid providing a 2 T axial magnetic field, and by a fine-granularity lead/liquid-argon (LAr) electromagnetic (EM) calorimeter covering $|\eta| < 3.2$. Hadronic calorimetry is provided by a steel/scintillator-tile calorimeter in the central pseudorapidity range ($|\eta| < 1.7$). The endcap and forward regions are instrumented with LAr calorimeters for both the EM and hadronic energy measurements up to $|\eta| = 4.9$. The muon spectrometer (MS) surrounds the calorimeters and is based on three large superconducting air-core toroidal magnets with eight coils each. Three layers of high-precision tracking chambers provide coverage in the range of $|\eta| < 2.7$, while dedicated fast chambers allow triggering in the region $|\eta| < 2.4$. A two-level trigger system [31], consisting of a hardware-based first-level trigger followed by a software-based high-level trigger (HLT), is used to select events. An extensive software suite [32] is used in data simulation, in the reconstruction and analysis of real and simulated data, in detector operations, and in the trigger and data acquisition systems of the experiment.

3 Data and simulation samples

The data used in this search correspond to an integrated luminosity of 139 fb^{-1} of pp collision data collected by the ATLAS detector between 2015 and 2018 at a centre-of-mass energy $\sqrt{s} = 13$ TeV. The uncertainty in the combined 2015–2018 integrated luminosity is 1.7% [33], obtained using the LUCID-2 detector [34] for the primary luminosity measurements. The presence of additional interactions in the same

[1] ATLAS uses a right-handed coordinate system with its origin at the nominal interaction point (IP) in the centre of the detector and the z-axis along the beam pipe. The x-axis points from the IP to the centre of the LHC ring, and the y-axis points upwards. Cylindrical coordinates (r, ϕ) are used in the transverse plane, ϕ being the azimuthal angle around the z-axis. The pseudorapidity is defined in terms of the polar angle θ as $\eta = -\ln\tan(\theta/2)$. Angular distance is measured in units of $\Delta R \equiv \sqrt{(\Delta\eta)^2 + (\Delta\phi)^2}$.

or neighbouring bunch crossing, referred to as pile-up, is characterised by the average number of such interactions, $\langle\mu\rangle$, which was 33.7 for the combined data sample. Only events recorded under stable beam conditions and for which all relevant detector subsystems were known to be in a good operating condition are used.

Dedicated Monte Carlo (MC) simulated samples are used to model SM processes and estimate the expected signal yields. All samples were passed through the full ATLAS detector simulation [35] based on GEANT4 [36], except for the signal samples that use a parameterised fast simulation of the calorimeter response [37] and GEANT4 for the other detector systems. The simulated events were reconstructed with the same algorithms as used for data. They contain a realistic modelling of pile-up interactions with pile-up profiles matching the ones of each data sample between 2015 and 2018, obtained by overlaying minimum-bias events simulated using the soft QCD processes of Pythia 8.186 [38] with the NNPDF2.3 leading-order (LO) [39] set of parton distribution functions (PDFs) and the A3 [40] set of tuned parameters (tune). The MC samples are corrected to account for differences between simulation and data in terms of the pile-up, the energy and momentum scales, and the reconstruction and identification efficiencies of physics objects.

Simulated events with pair-produced up-type ($Q = +\frac{2}{3}$) scalar LQs were generated at next-to-leading order (NLO) in QCD with MADGRAPH5_AMC@NLO v2.6.0 [41], using the LQ model of Ref. [42], in which fixed-order NLO QCD calculations [43, 44] are interfaced to PYTHIA 8.230 [45] for the parton shower (PS) and hadronisation. Parton luminosities were provided by the five-flavour scheme NNPDF3.0 NLO [46] PDF set with $\alpha_s = 0.118$ and the underlying event (UE) was modelled with the A14 tune [47, 48]. The coupling parameter λ was set to 0.3, resulting in a relative LQ width of approximately 0.2% and ensuring the LQs decay promptly. In all cases, $\beta = 0.5$ such that the couplings to charged leptons and neutrinos were equal and the decay products were interfaced to MADSPIN [49] to preserve spin correlations. Different values for $\mathcal{B}$ were then obtained by reweighting the simulated events according to the generator information about their decay following the procedure in Ref. [18]. Signal cross-sections were obtained from the calculation of the pair production of scalar coloured particles, such as the hypothesised supersymmetric partner of the top quark, as these particles have the same production modes and their pair-production cross-section depends only on their mass. These processes were computed at approximate next-to-next-to-leading order (NNLO) in QCD with resummation of next-to-next-to-leading-logarithmic (NNLL) soft gluon terms [50–53]. The cross-sections do not include contributions from t-channel lepton exchange, which are neglected in Ref. [42] and may lead to corrections at the percent level [54]. The nominal cross-section and its uncertainty were derived using the PDF4LHC15_mc PDF set, following the recommendations of Ref. [55]. For LQ masses between 300 GeV and 2000 GeV, the cross-sections range from 10 pb to 0.01 fb.

Simulated events with pair-produced up-type vector LQs were generated at LO in QCD with MADGRAPH5_AMC@NLO v2.6.0, using the LQ model of Ref. [16] and the NNPDF3.0 NLO PDF set with $\alpha_s = 0.118$. Decays of the LQs were performed with MADSPIN, while PS and hadronisation were simulated using PYTHIA 8.244 with the A14 tune. The full model includes two additional vector states that are necessary to obtain a realistic extension of the SM, a colour singlet Z' and a colour octet G'. However, these are not present in the MADGRAPH model and hence do not contribute to the Feynman diagrams considered for pair production of vector leptoquarks. The samples were produced with a coupling strength $g_U = 3.0$, where g_U represents the overall coupling between the LQ and the fermion, motivated by a suppression of the production cross-section for the additional mediators in the ultraviolet completion of the model, which might otherwise be in tension with existing LHC limits. This choice of coupling results in a relative LQ width of around 10%. In all cases, $\beta = 0.5$ and the same reweighting as in the scalar LQ case is

then used to probe different $\mathcal{B}$ values. As mentioned, the model introduces two different coupling scenarios the minimal-coupling scenario and the Yang–Mills scenario. In the latter case the LQ is a massive gauge boson and has additional couplings to the SM gauge bosons, resulting in enhanced cross-sections. Since no higher-order cross-sections are available for this model, the LO MadGraph5_aMC@NLO cross-sections were used and vary between 94 pb (340 pb) and 0.05 fb (0.61 fb) for LQ masses between 300 GeV and 2000 GeV in the minimal-coupling (Yang–Mills) case. Above 500 GeV, kinematic differences between the two scenarios are negligible.

Scalar (vector) LQ samples were produced with LQ masses between 300 GeV to 2000 GeV, with a mass interval of 50 GeV in the range of 800–1600 GeV (1400–1600 GeV) and 100 GeV otherwise.

Table 1: The list of generators used for the simulation of the SM background processes. Information is given on the matrix element (ME) generator (including the perturbative QCD order), the PDF set, the parton shower (PS) and the underlying event (UE). The perturbative order (in QCD unless otherwise specified) of the cross-section used to normalise the different samples is also presented. (§) The $t\bar{t} - Wt$ interference was handled using the diagram removal scheme. (†) The cross-sections from Sherpa at NLO were used to normalise the WW, WZ, ZZ and $t\bar{t}W/Z$ events. (‡) The $qq \to ZH$ process was normalised to the NNLO (QCD) + NLO(EW) cross-section for the $pp \to ZH$ process [56–61], after subtracting the $gg \to ZH$ contribution.

Process	ME generator	ME QCD order	ME PDF	PS and hadronisation	UE tune	Cross-section order
Top-quark						
$t\bar{t}^{(\S)}$	Powheg-Box v2 [62]	NLO	NNPDF3.0NLO	Pythia 8.230	A14	NNLO+NNLL [63]
t-channel	Powheg-Box v2	NLO	NNPDF3.0NLO	Pythia 8.230	A14	NLO [64]
s-channel	Powheg-Box v2	NLO	NNPDF3.0NLO	Pythia 8.230	A14	NLO [65]
$Wt^{(\S)}$	Powheg-Box v2	NLO	NNPDF3.0NLO	Pythia 8.230	A14	NLO [66]
Top-quark + W/Z						
$t\bar{t}Z$	Sherpa 2.2.1 [67–69]	NLO	NNPDF3.0NNLO	Sherpa 2.2.1	Default	NLO$^{(\dagger)}$
$t\bar{t}W$	Sherpa 2.2.8	NLO	NNPDF3.0NNLO	Sherpa 2.2.8	Default	NLO$^{(\dagger)}$
Vector boson + jets						
W/Z+jets	Sherpa 2.2.1	NLO ($\leq$ 2 jets) LO (3,4 jets)	NNPDF3.0NNLO	Sherpa 2.2.1	Default	NNLO [70]
Diboson						
WW, WZ, ZZ	Sherpa 2.2.1	NLO ($\leq$ 1 jet) LO (2,3 jets)	NNPDF3.0NNLO	Sherpa 2.2.1	Default	NLO$^{(\dagger)}$
Higgs boson						
ggF	Powheg-Box v2	NNLO	NNPDF3.0NLO	Pythia 8.212	AZNLO [71]	N3LO(QCD)+NLO(EW) [72–76]
VBF	Powheg-Box v2	NLO	NNPDF3.0NLO	Pythia 8.212	AZNLO	NNLO(QCD)+NLO(EW) [72, 77–79]
$qq \to WH$	Powheg-Box v2	NLO	NNPDF3.0NLO	Pythia 8.212	AZNLO	NNLO(QCD)+NLO(EW) [56–59, 61, 80]
$qq \to ZH$	Powheg-Box v2	NLO	NNPDF3.0NLO	Pythia 8.212	AZNLO	NNLO(QCD)+NLO(EW)$^{(\ddagger)}$
$gg \to ZH$	Powheg-Box v2	NLO	NNPDF3.0NLO	Pythia 8.212	AZNLO	NLO+NLL [81–85]
$t\bar{t}H$	Powheg-Box v2	NLO	NNPDF3.0NLO	Pythia 8.230	A14	NLO [72]

Background samples were simulated using different MC event generators depending on the process. All background processes are normalised to the most accurate available theoretical calculation of their respective cross-sections. The most relevant event generators, the accuracy of theoretical cross-sections, the UE parameter tunes, and the PDF sets used in simulating the SM background processes are summarised in Table 1. For all samples, except those generated using Sherpa, the EvtGen v1.2.0 [86] program was used to simulate the properties of the b- and c-hadron decays.

4 Event reconstruction and object definitions

The LQ signature of interest in this search gives rise to a set of reconstructed objects that consist primarily of τ-leptons, which may decay into light leptons or hadronically, and jets from the hadronisation of quarks, specifically b-quarks. In addition, neutrinos produced in the decay of τ-leptons and the semileptonic decay of b-hadrons contribute to the missing transverse momentum $\boldsymbol{p}_{\mathrm{T}}^{\mathrm{miss}}$ of the event. To be considered for analysis, events are required to have at least one pp interaction vertex, reconstructed from two or more charged-particle tracks with $p_{\mathrm{T}} > 500\,\mathrm{MeV}$; the one with the highest summed p_{T}^2 of associated tracks is selected as the primary vertex.

Electron candidates are reconstructed by matching ID tracks to energy clusters in the EM calorimeter. They must satisfy $p_{\mathrm{T}} > 7\,\mathrm{GeV}$ and lie in the range of $|\eta| < 2.47$, excluding the transition region between the barrel and endcap detectors ($1.37 < |\eta| < 1.52$). Electrons are further identified using a likelihood-based method, based on the track quality, the profile of the shower measured in the EM calorimeter and the consistency between the track and the energy cluster [87]. Two identification criteria are used to select electrons in this analysis: 'veto electrons' are required to satisfy the 'loose' identification working point, while 'signal electrons' are required to satisfy the more stringent 'tight' working point.

Muon candidates are reconstructed from tracks in the MS, matched with compatible tracks in the ID where coverage allows; in regions where the MS is only partially instrumented ($|\eta| < 0.1$) an energy deposit in the calorimeter compatible with a minimum-ionising particle is combined with a compatible ID track instead. They must satisfy $p_{\mathrm{T}} > 7\,\mathrm{GeV}$ and lie in the range of $|\eta| < 2.7$. Muons are further identified based on the number of hits in the various ID subdetectors and MS stations, the compatibility between the measurements in the two detectors and the properties of the resulting track fit. Two identification criteria [88] are used to select muons: 'veto muons' must satisfy a 'loose' identification requirement, while the 'signal muons' are required to satisfy the 'medium' ('high-p_{T}') working point if the p_{T} is less than (greater than) 800 GeV. The more stringent high-p_{T} requirements remove around 20% of muons but improve the p_{T} resolution by $\approx 30\%$ above 1.5 TeV, significantly suppressing potential backgrounds [89].

To suppress misidentified leptons or those arising from hadron decays, all light-lepton candidates must satisfy an isolation criterion that limits the presence of tracks (calorimeter deposits) in a p_{T}-dependent (fixed) radius cone. The resulting efficiency is above 99% for both electrons and muons in the signal regions. Finally, signal leptons must satisfy stricter requirements on their transverse momenta depending on the data-taking period, as detailed in Section 5.

Jets are reconstructed from topological energy clusters and charged-particle tracks, resulting from a particle-flow algorithm [90], using the anti-k_t algorithm with a radius parameter of $R = 0.4$ [91, 92]. They are required to satisfy $p_{\mathrm{T}} > 20\,\mathrm{GeV}$ and lie in the range of $|\eta| < 2.5$. To suppress jets from pile-up, jets with $p_{\mathrm{T}} < 60\,\mathrm{GeV}$ and $|\eta| < 2.4$ are required to originate from the primary vertex using a multivariate 'jet vertex tagger' [93]. A multivariate algorithm based on a deep neural network, known as the 'DL1r tagger' [94–96], is used to identify jets containing b-hadrons (b-jets) based on the jet kinematics, the impact parameters of tracks associated with the jet and the reconstruction of displaced vertices. This analysis uses a working point with a 77% efficiency for true b-jets and corresponding rejection factors for light-flavour jets, charm jets and τ-leptons, measured in simulated $t\bar{t}$ events, of 170, 5 and 21, respectively [97, 98].

Hadronically decaying τ-lepton candidates are seeded by jets, which are required to have one or three associated tracks (referred to hereafter as 'one-prong' or 'three-prong' candidates, respectively) with a total charge of ± 1 [99]. The transverse momentum of the visible decay products ($\tau_{\text{had-vis}}$) must satisfy $p_{\mathrm{T}} > 20\,\mathrm{GeV}$ and lie in the range of $|\eta| < 2.47$, excluding the transition region defined above. True $\tau_{\text{had-vis}}$

candidates are discriminated from quark- and gluon-initiated jets via a recurrent neural network (RNN) using calorimeter- and tracking-based variables as input and trained separately on one- and three-prong candidates [100]. The 'loose' working point used has an efficiency of approximately 85% and 75% for one- and three-prong $\tau_{\text{had-vis}}$ respectively. A further boosted decision tree (BDT) is used to reject one-prong $\tau_{\text{had-vis}}$ candidates originating from electrons with an efficiency of about 95% [101]. For the estimation of the background from jets misidentified as $\tau_{\text{had-vis}}$ (described in Section 6), anti-$\tau_{\text{had-vis}}$ candidates are defined in the same way as above but are required to fail to satisfy the nominal loose RNN working point requirements and instead satisfy a looser requirement that has an efficiency of 99% for selecting true $\tau_{\text{had-vis}}$ candidates.

The $\boldsymbol{p}_{\text{T}}^{\text{miss}}$ (with magnitude $E_{\text{T}}^{\text{miss}}$) is computed from the negative vectorial sum of the selected and calibrated objects described above, along with an extra track-based 'soft term' to account for the energy of particles originating from the primary vertex but not associated to any of the reconstructed objects [102, 103].

To resolve ambiguities whereby the same detector signature may be reconstructed as more than one physics object, a sequential overlap-removal procedure is applied. First, electron candidates are discarded if they share a track with a more energetic electron or a muon identified in the MS; if the muon is identified in the calorimeter it is removed instead. Any $\tau_{\text{had-vis}}$ candidate within $\Delta R = 0.2$ of an electron or a muon (which must be reconstructed in the MS if the $\tau_{\text{had-vis}}$ p_{T} is above 50 GeV) is then rejected. Jets are discarded if they lie within $\Delta R = 0.2$ of an electron or have fewer than three associated tracks and lie within the same distance of a muon. Electron or muon ($\tau_{\text{had-vis}}$) candidates within $\Delta R = 0.4$ ($\Delta R = 0.2$) of any remaining jet are then removed. Finally, ambiguities between anti-$\tau_{\text{had-vis}}$ candidates and jets within $\Delta R = 0.2$ are resolved in favour of the jet if it is b-tagged or the anti-$\tau_{\text{had-vis}}$ otherwise.

5 Event selection

The event selection targets a signature consisting of a pair of τ-leptons and a pair of b-quarks. It splits the events into two orthogonal signal categories based on the τ-lepton decay mode: the $\tau_{\text{lep}}\tau_{\text{had}}$ channel, which selects events with a light lepton, an oppositely charged $\tau_{\text{had-vis}}$ and one or two b-jets, and the $\tau_{\text{had}}\tau_{\text{had}}$ channel, which selects events with two opposite-charge $\tau_{\text{had-vis}}$ and one or two b-jets. Multivariate techniques are used to search for a LQ-pair signal in the two signal regions (SRs).

5.1 Signal regions

Candidate events were recorded using a combination of single-lepton [104, 105] and single-$\tau_{\text{had-vis}}$ triggers [106]. The single-lepton trigger used in the $\tau_{\text{lep}}\tau_{\text{had}}$ channel required a reconstructed light lepton at the HLT, with a minimum E_{T} threshold ranging from 24 to 26 GeV for electrons and a minimum p_{T} threshold ranging from 20 to 25 GeV for the muons, depending on the data-taking period. Offline leptons are required to be geometrically matched to the corresponding trigger object and have a p_{T} threshold 1–2 GeV above the HLT threshold in order to operate in the region where the trigger was fully efficient. The single-$\tau_{\text{had-vis}}$ triggers used in the $\tau_{\text{had}}\tau_{\text{had}}$ channel required a reconstructed HLT $\tau_{\text{had-vis}}$ with a period-dependent minimum p_{T} threshold ranging between 80 GeV and 160 GeV. The corresponding p_{T}-threshold for the offline $\tau_{\text{had-vis}}$, which is again required to be geometrically matched to the trigger object, ranges between 100 GeV and 180 GeV, while the non-trigger-matched $\tau_{\text{had-vis}}$ is required to have $p_{\text{T}} > 20$ GeV.

Following the trigger selection, the $\tau_{\text{lep}}\tau_{\text{had}}$ category requires exactly one 'signal' light lepton and an oppositely charged $\tau_{\text{had-vis}}$, while the $\tau_{\text{had}}\tau_{\text{had}}$ category requires exactly two opposite-charge $\tau_{\text{had-vis}}$ and no 'veto' light leptons. Both categories require at least two jets, one or two of which must be b-tagged, with $p_{\text{T}} > 45$ (20) GeV for the leading (sub-leading) jet.

The invariant mass of the two τ-lepton decay products is an important variable with which to reject the Z+jets background. It is calculated using the missing mass calculator (MMC) [107], with the light lepton and the $\tau_{\text{had-vis}}$ (two $\tau_{\text{had-vis}}$) and the $\boldsymbol{p}_{\text{T}}^{\text{miss}}$ as input in the $\tau_{\text{lep}}\tau_{\text{had}}$ ($\tau_{\text{had}}\tau_{\text{had}}$) category, and it is required to satisfy $m_{\tau\tau}^{\text{MMC}} \notin 40 - 150\,\text{GeV}$. Two further selections are applied to target the characteristic LQ signature while reducing the large multi-jet background. The scalar sum of the transverse momenta (s_{T}), calculated taking into account the light lepton, $\tau_{\text{had-vis}}$, two leading jets and the $E_{\text{T}}^{\text{miss}}$, is a powerful discriminator. It is required to satisfy $s_{\text{T}} > 600\,\text{GeV}$, while the $E_{\text{T}}^{\text{miss}}$ itself is required to exceed 100 GeV.

The full event selection is summarised in Table 2 and the resulting acceptance times efficiency is shown in Figure 2 as a function of m_{LQ}. Since the analysis prioritises high mass LQs that have not yet been excluded in the benchmark models under consideration, it is not optimal for low LQ masses.

Table 2: Summary of the event selections for the $\tau_{\text{lep}}\tau_{\text{had}}$ and $\tau_{\text{had}}\tau_{\text{had}}$ categories. Where two objects are required, the thresholds on the sub-leading object are given in parenthesis. Where the selection depends on data-taking period, the different possible threshold values are separated by commas.

	$\tau_{\text{lep}}\tau_{\text{had}}$ channel	$\tau_{\text{had}}\tau_{\text{had}}$ channel
e/μ selection	$= 1$ 'signal' e or μ $p_{\text{T}}^{e} > 25, 27\,\text{GeV}$ $p_{\text{T}}^{\mu} > 21, 27\,\text{GeV}$	No 'veto' e or μ
$\tau_{\text{had-vis}}$ selection	$= 1$ $\tau_{\text{had-vis}}$ $p_{\text{T}}^{\tau} > 100\,\text{GeV}$	$= 2$ $\tau_{\text{had-vis}}$ $p_{\text{T}}^{\tau} > 100, 140, 180$ (20) GeV
Jet selection	≥ 2 jets $p_{\text{T}}^{\text{jet}} > 45$ (20) GeV 1 or 2 b-jets	
Additional selection	Opposite charge $e, \mu, \tau_{\text{had}}$ and τ_{had} $m_{\tau\tau}^{\text{MMC}} \notin 40 - 150\,\text{GeV}$ $E_{\text{T}}^{\text{miss}} > 100\,\text{GeV}$ $s_{\text{T}} > 600\,\text{GeV}$	

5.2 Multivariate signal extraction

Following the event selection, the LQ signal is extracted using a multivariate discriminant. To obtain near-optimal sensitivity and continuity over the full range of LQ masses considered, a parameterised neural network (PNN) [108], parameterised in terms of the generated LQ mass, is chosen. The PNN consists of three hidden layers, each with 32 nodes, implemented in Keras [109] with the Tensorflow [110] backend.

The PNN inputs consist of a combination of multiplicity, kinematic and angular quantities that discriminate between the signal and the dominant background. In the case of the $b\tau$ invariant mass, the most likely

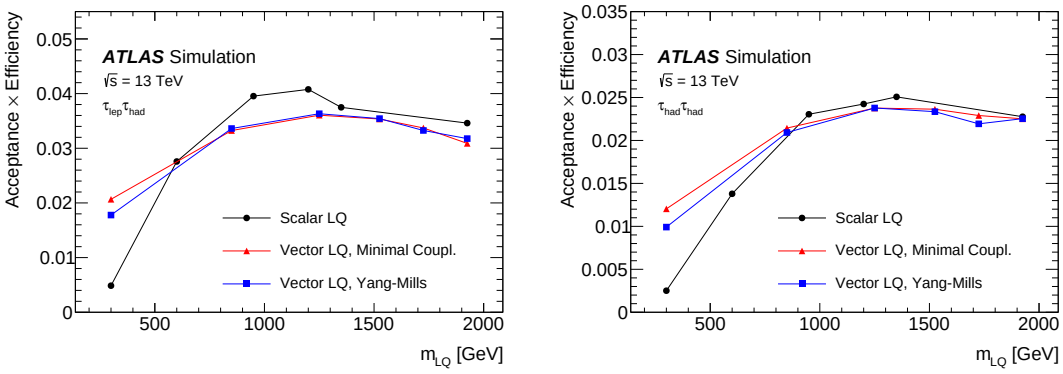

(a) (b)

Figure 2: The expected acceptance times efficiency for the scalar and vector LQs, with both the minimal-coupling and the Yang–Mills scenarios, at $\beta = 0.5$ as a function of m_{LQ} in the (a) $\tau_{\mathrm{lep}}\tau_{\mathrm{had}}$ and (b) $\tau_{\mathrm{had}}\tau_{\mathrm{had}}$ channels. The values include the leptonic and hadronic branching ratios of the tau lepton.

combination of the τ-lepton and a b-jet[2] is chosen based on a mass-pairing strategy that minimises the mass difference between the two resulting LQ candidates. The variables, which are similar for both the $\tau_{\mathrm{lep}}\tau_{\mathrm{had}}$ and $\tau_{\mathrm{had}}\tau_{\mathrm{had}}$ categories, are summarised in Table 3 and defined as follows:

- $\tau_{\text{had-vis}}$ p_{T}^{0} is the transverse momentum of the highest-p_{T} $\tau_{\text{had-vis}}$;
- s_{T} is the scalar sum of the transverse momenta defined above;
- $N_{b-\text{jets}}$ is the number of b-jets;
- $m(\tau, \text{jet})_{0,1}$ are the larger (0) and smaller (1) of the two LQ masses obtained via the mass-pairing strategy ($\tau_{\mathrm{had}}\tau_{\mathrm{had}}$ channel only);
- $m(\ell, \text{jet})$ and $m(\tau_{\mathrm{had}}, \text{jet})$ are the mass of the light-lepton or $\tau_{\text{had-vis}}$, respectively, combined with its mass-paired b-jet ($\tau_{\mathrm{lep}}\tau_{\mathrm{had}}$ channel only);
- $\Delta R(\ell, \text{jet})$ ($\Delta R(\tau_{\mathrm{had}}, \text{jet})$) is the ΔR between the light lepton (leading $\tau_{\text{had-vis}}$) and the mass-paired jet in the $\tau_{\mathrm{lep}}\tau_{\mathrm{had}}$ ($\tau_{\mathrm{had}}\tau_{\mathrm{had}}$) category;
- $\Delta\phi(\ell, E_{\mathrm{T}}^{\mathrm{miss}})$ is the azimuthal opening angle between the lepton and the $E_{\mathrm{T}}^{\mathrm{miss}}$ ($\tau_{\mathrm{lep}}\tau_{\mathrm{had}}$ category only);
- $E_{\mathrm{T}}^{\mathrm{miss}}$ ϕ centrality quantifies the transverse direction of the $\boldsymbol{p}_{\mathrm{T}}^{\mathrm{miss}}$ relative to the light lepton and $\tau_{\text{had-vis}}$ (two $\tau_{\text{had-vis}}$) in the $\tau_{\mathrm{lep}}\tau_{\mathrm{had}}$ ($\tau_{\mathrm{had}}\tau_{\mathrm{had}}$) category and is defined in Ref. [111].

A selection of representative input distributions, after the background corrections described in Section 6, are presented in Figures 3 and 4 for the $\tau_{\mathrm{lep}}\tau_{\mathrm{had}}$ SR and the $\tau_{\mathrm{had}}\tau_{\mathrm{had}}$ SR, respectively. While the relative importance of the variables varies with LQ mass, the s_{T} and mass variables are generally the most performant. The resulting PNN score distributions, which peak at higher values for LQ signals than the background processes, are used as the final analysis discriminant.

[2] In the case of only one b-jet, the highest-p_{T} non-b-jet is taken as the second jet.

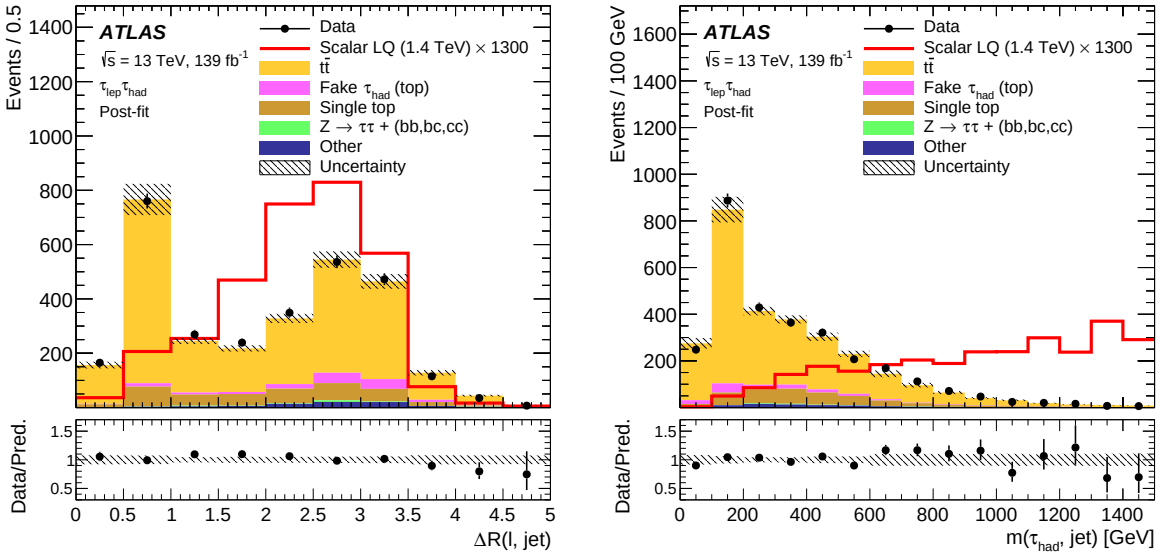

(a) (b)

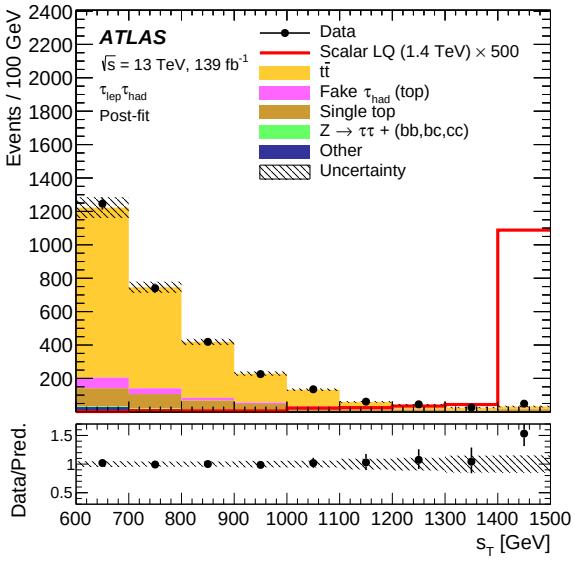

(c)

Figure 3: Signal (solid lines), post-fit background (filled histograms) and data (dots with error bars) distributions of representative PNN input variables in the $\tau_{\text{lep}}\tau_{\text{had}}$ SR: (a) $\Delta R(\ell, \text{jet})$, (b), $m(\tau_{\text{had}}, \text{jet})$ and (c) s_{T}. The normalisation and shape of the backgrounds are determined from the background-only likelihood fit to data and the ratios of the data to the sum of the predicted backgrounds are shown in the lower panels. 'Other' refers to the sum of minor backgrounds (vector boson + jets, diboson and Higgs boson). The hatched band indicates the combined statistical and systematic uncertainty in the total background prediction. The expected signal for a 1.4 TeV scalar LQ, scaled by the indicated factor for visibility, is overlaid. The last bin includes the overflow.

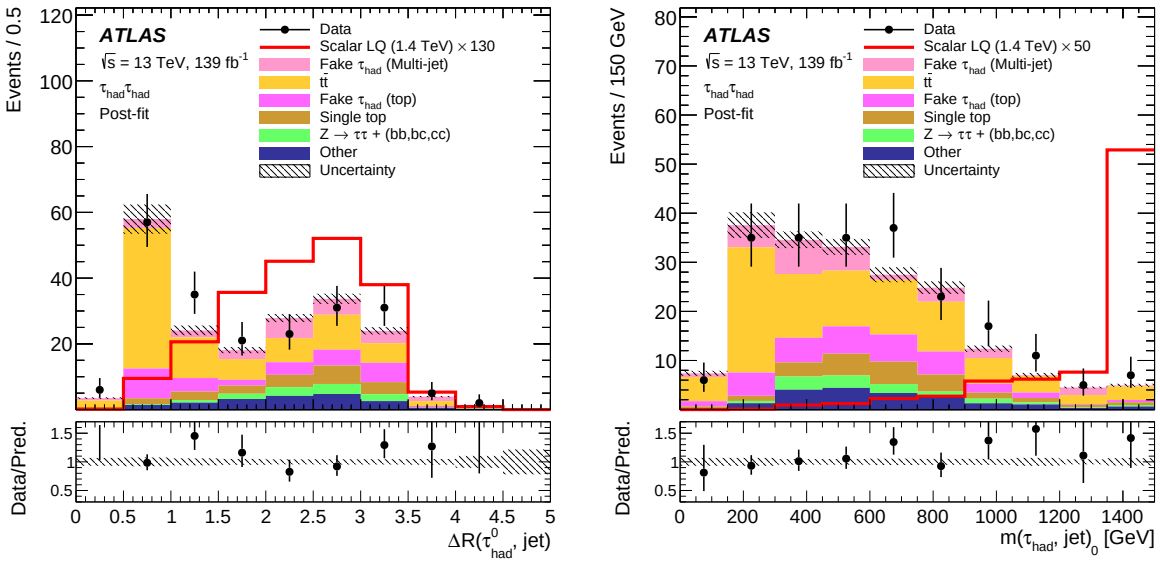

(a) (b)

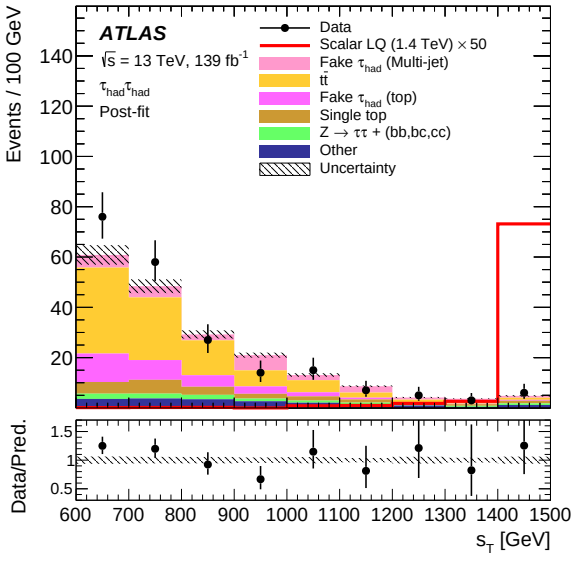

(c)

Figure 4: Signal (solid lines), post-fit background (filled histograms) and data (dots with error bars) distributions of representative PNN input variables in the $\tau_{\text{had}}\tau_{\text{had}}$ SR: (a) $\Delta R(\tau^0_{\text{had}}, \text{jet})$ where τ^0_{had} is the leading τ-lepton, (b) the larger of the two τ-jet mass combinations $m(\tau_{\text{had}}, \text{jet})_0$ and (c) s_{T}. The normalisation and shape of the backgrounds are determined from the background-only likelihood fit to data and the ratios of the data to the sum of the predicted backgrounds are shown in the lower panels. 'Other' refers to the sum of minor backgrounds (vector boson + jets, diboson and Higgs boson). The hatched band indicates the combined statistical and systematic uncertainty in the total background prediction. The expected signal for a 1.4 TeV scalar LQ, scaled by the indicated factor for visibility, is overlaid. The last bin includes the overflow.

Table 3: Summary of variables used as inputs to the PNN in the $\tau_{\text{lep}}\tau_{\text{had}}$ and $\tau_{\text{had}}\tau_{\text{had}}$ categories. The variables are defined in the text.

Variable	$\tau_{\text{lep}}\tau_{\text{had}}$ channel	$\tau_{\text{had}}\tau_{\text{had}}$ channel
$\tau_{\text{had-vis}}$ p_{T}^{0}	✓	✓
s_{T}	✓	✓
$N_{b-\text{jets}}$	✓	✓
$m(\tau, \text{jet})_{0,1}$		✓
$m(\ell, \text{jet})$, $m(\tau_{\text{had}}, \text{jet})$	✓	
$\Delta R(\tau, \text{jet})$	✓	✓
$\Delta\phi(\ell, E_{\text{T}}^{\text{miss}})$	✓	
$E_{\text{T}}^{\text{miss}}$ ϕ centrality	✓	✓

The PNNs are trained on all scalar LQ signal masses simultaneously against the main $t\bar{t}$ and single-top backgrounds, taking into account both the true and misidentified $\tau_{\text{had-vis}}$ components with the latter corrected as described in Section 6. The same PNN training is used for both vector LQ models since separate trainings were found to provide a negligible improvement in sensitivity. For the signals, the generated LQ mass is used as the parameterisation input in addition to the input variables described above, while in the case of the backgrounds a mock LQ mass is randomly assigned from the range of signal LQ masses such that the resulting training is independent of the mass. In all cases, the input variables are standardised by subtracting the median value and dividing by the interquartile range. The resulting PNN score distributions are used as the final analysis discriminants.

6 Background modelling

The dominant background in the $\tau_{\text{had}}\tau_{\text{had}}$ and $\tau_{\text{lep}}\tau_{\text{had}}$ channels is top production, including $t\bar{t}$ and single-top-quark production. A subdominant background is Z boson production in association with heavy-flavour quarks (bb, bc, cc), termed Z + HF hereafter. Both top production and Z + HF are estimated from simulation to which data-driven corrections are applied. In the $\tau_{\text{had}}\tau_{\text{had}}$ channel, multi-jet events form a non-negligible background that is estimated by using data-driven techniques. Small contributions to the background from all other processes are estimated by using simulated events. This section describes the background estimation methods used for top-quark-pair and single-top backgrounds, multi-jet backgrounds, and the Z + HF background. The background is validated for $\tau_{\text{had}}\tau_{\text{had}}$ and $\tau_{\text{lep}}\tau_{\text{had}}$ events in a region with an inverted s_{T} selection, as well as a region with a low PNN score and the signal region selection. In addition, the $\tau_{\text{had}}\tau_{\text{had}}$ multi-jet estimate is validated in a region where the two $\tau_{\text{had-vis}}$ have the same electric charge. The potential signal contamination in all regions described in this section is negligible.

The process of estimating the backgrounds follows several steps. First, an overall shape correction is determined for the top background, as described in Section 6.1.1. Then, with this in place, a shape and normalisation correction is determined for the top backgrounds with jets misidentified as $\tau_{\text{had-vis}}$, as described in Section 6.1.2. After applying these corrections, a prediction for the shape and normalisation of multi-jet backgrounds is determined for the $\tau_{\text{had}}\tau_{\text{had}}$ channel in Section 6.2. Finally, with all relevant corrections in place, a normalisation factor is determined for the Z + HF backgrounds, as described in Section 6.3. The resulting corrections are only weakly coupled due to the high purity of each control

region, meaning that corrections for a specific background process do not significantly affect the overall background in control regions targeting other backgrounds. All of these corrections are applied in the final SR fit.

6.1 Top quark backgrounds

For top-quark-pair and single-top-quark production (top backgrounds), events are estimated separately based on whether the $\tau_{\text{had-vis}}$ candidate in the event is correctly identified (referred to as a true $\tau_{\text{had-vis}}$) or whether it is a quark- or gluon-initiated jet misidentified as a $\tau_{\text{had-vis}}$ (referred to as a fake $\tau_{\text{had-vis}}$). The small contributions from light leptons that are misidentified as $\tau_{\text{had-vis}}$ are considered together with the true $\tau_{\text{had-vis}}$ contribution. Events with a true $\tau_{\text{had-vis}}$ and a hadronic jet misidentified as a light lepton contribute negligibly to the $\tau_{\text{lep}}\tau_{\text{had}}$ channel and are not considered.

These backgrounds are estimated in a multi-step data-driven process that is applied to simulated events. First, all top backgrounds are scaled by an s_{T}-dependent reweighting factor (RF), and then simulated background events with misidentified $\tau_{\text{had-vis}}$ are further corrected by a scale factor (SF) that is binned in the $\tau_{\text{had-vis}}$ transverse momentum.

6.1.1 Overall reweighting of top backgrounds

The motivation for scaling the $t\bar{t}$ and single-top backgrounds arises from mismodelling of the data by simulation observed in control regions (CRs). It is seen that this effect becomes more pronounced for events with higher momentum top quarks, which is where this analysis is primarily focused. This mismodelling has also been observed in ATLAS measurements of the $t\bar{t}$ differential cross-section, where it is seen that the number of events is overestimated at high top-quark p_{T} [112–114].

For this reason, a CR is defined to determine a binned shape and normalisation correction of the simulated top quark events to data. Events in this CR are required to have two b-jets with p_{T} greater than 45 and 20 GeV, exactly two light leptons with opposite charge, $E_{\text{T}}^{\text{miss}} > 100$ GeV, and a dilepton mass $(m_{\ell\ell}) > 110$ GeV. They are also required to have $m_{b\ell} > 250$ GeV, where $m_{b\ell} = \min(\max(m_{b_0\ell_0}, m_{b_1\ell_1}), \max(m_{b_0\ell_1}, m_{b_1\ell_0}))$, where the 0 and 1 indices refer to the leading and sub-leading b-tagged jets and leptons in order of transverse momentum. This region is orthogonal to the SRs and is over 99% pure in $t\bar{t}$ events.

The RFs are derived by subtracting all non-top backgrounds, as estimated using simulation, from data. A ratio of the remaining events to the prediction of $t\bar{t}$ and single-top events in simulation is then calculated. This factor is binned in s_{T}, with one bin up to 400 GeV, steps of 100 GeV from 400 to 1400 GeV, and then one bin for values greater than 1400 GeV. The values of the RFs decrease from 0.97 at low s_{T} to approximately 0.62 in the highest s_{T} bin. Even in the highest s_{T} bin, the signal contamination remains at the percent level. The largest relative contribution of single-top events is also at high s_{T}. This reweighting is applied in both the $\tau_{\text{lep}}\tau_{\text{had}}$ and $\tau_{\text{had}}\tau_{\text{had}}$ SRs for $t\bar{t}$ and single-top events with true and misidentified τ-leptons, as well as in all CRs. The uncertainty in this RF is taken from the statistical uncertainty in the factor, bin-by-bin in s_{T}, and its impact on the shape and normalisation of the final PNN score distribution are considered. In addition, top background modelling uncertainties are propagated through the reweighting process, so that modified RFs are applied when evaluating such uncertainties in the final fit.

6.1.2 Top backgrounds with jets misidentified as $\tau_{\text{had-vis}}$

In addition to this overall RF, the estimation of top backgrounds with jets misidentified as $\tau_{\text{had-vis}}$ in the SRs is performed using simulated events with additional data-driven corrections. A fit is performed in a $\tau_{\text{lep}}\tau_{\text{had}}$-based CR to simultaneously correct the overall normalisation of true $\tau_{\text{had-vis}}$ and misidentified $\tau_{\text{had-vis}}$ events while deriving an SF to be applied to misidentified $\tau_{\text{had-vis}}$ events in the $\tau_{\text{lep}}\tau_{\text{had}}$ and $\tau_{\text{had}}\tau_{\text{had}}$ SRs. The RF for top backgrounds is applied to this CR before the fit. The SFs obtained are then applied in the SRs, in order to correct the $\tau_{\text{had-vis}}$ misidentification rate in simulation to that observed in data.

The CR has the same selection as the SR for the $\tau_{\text{lep}}\tau_{\text{had}}$ channel, except that the $\tau_{\text{had-vis}}$ $p_{\text{T}} > 100$ GeV requirement is removed and s_{T} is required to be in a range of 400–600 GeV. This region is 97% pure in $t\bar{t}$ events, with a mixture of both correctly identified and misidentified $\tau_{\text{had-vis}}$ that varies with $\tau_{\text{had-vis}}$ p_{T}.

The distribution used for this estimation is the transverse mass of the light lepton and missing transverse momentum, defined as $m_{\text{T}}(\ell, E_{\text{T}}^{\text{miss}}) = \sqrt{(E_{\text{T}}^{\text{miss}} + p_{\text{T},\ell})^2 - (E_{\text{T},x}^{\text{miss}} + p_{x,\ell})^2 - (E_{\text{T},y}^{\text{miss}} + p_{y,\ell})^2}$. The expected shapes for top backgrounds with true and misidentified $\tau_{\text{had-vis}}$ in this distribution differ significantly, making it possible to constrain the two background sources. The normalisation of the true and misidentified $\tau_{\text{had-vis}}$ background is allowed to vary freely, and SFs for the misidentified $\tau_{\text{had-vis}}$ background are determined in bins of $\tau_{\text{had-vis}}$ p_{T}. All detector-related uncertainties and top background modelling uncertainties are included as nuisance parameters in the fit. An example fit in a single bin of p_{T} is shown in Figure 5 for the (a) $\tau_{\text{had-vis}}$ and (b) anti-$\tau_{\text{had-vis}}$ CRs. Depending on $\tau_{\text{had-vis}}$ p_{T}, the SFs run from 0.90 in the lowest p_{T} bin down to 0.56 in the highest p_{T} bin.

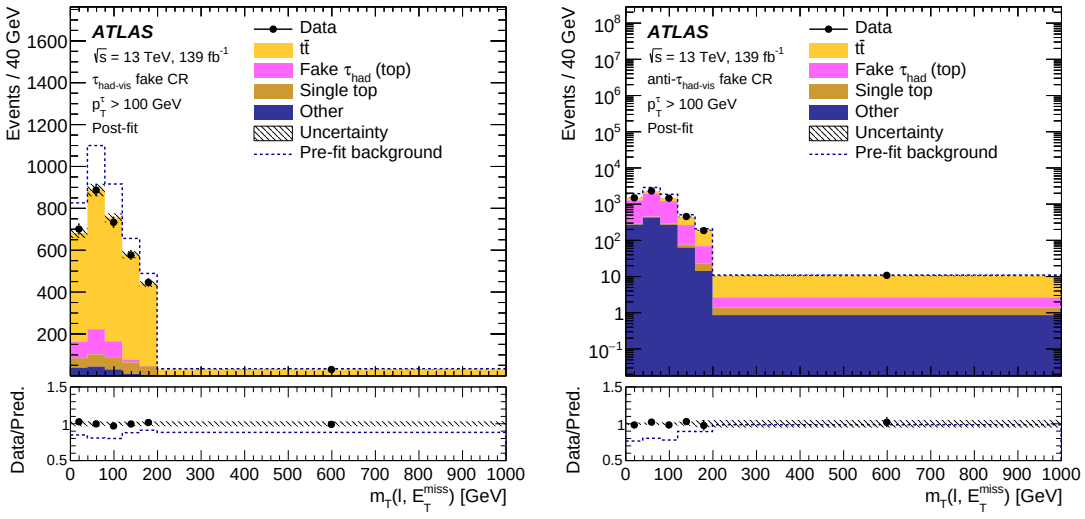

(a) (b)

Figure 5: Post-fit plots for true and misidentified $\tau_{\text{had-vis}}$ in (a) the $\tau_{\text{had-vis}}$ and (b) the anti-$\tau_{\text{had-vis}}$ CRs, in a single p_{T} bin ($\tau_{\text{had-vis}}$ p_{T} >100 GeV). 'Other' refers to the sum of minor backgrounds (vector boson + jets, diboson and Higgs boson). The lower panels show the ratios of the data to the sum of the predicted backgrounds. The hatched bands indicate the combined statistical and systematic uncertainty in the total background predictions. The dashed lines denote the total pre-fit backgrounds for comparison, while the last bins include the overflow.

For the estimation of top backgrounds with misidentified $\tau_{\text{had-vis}}$, an uncertainty is considered that arises from the limited number of events and an additional uncertainty is defined by comparing the nominal SFs

to SFs derived with a more inclusive s_{T} selection ($s_{\mathrm{T}} < 600$ GeV). This last uncertainty is intended to address a possible s_{T}-dependence in the mismodelling of top backgrounds. The difference between the central values for SFs measured with these two s_{T} selections is taken as the s_{T}-dependence uncertainty.

6.2 Multi-jet backgrounds with jets misidentified as $\tau_{\text{had-vis}}$

For the $\tau_{\mathrm{had}}\tau_{\mathrm{had}}$ channel, multi-jet processes can contribute to the SR at non-negligible levels. For this reason, the $\tau_{\mathrm{had}}\tau_{\mathrm{had}}$ channel uses a data-driven fake-factor (FF) method to estimate this background. These FFs are measured in a CR with the same selection as the $\tau_{\mathrm{had}}\tau_{\mathrm{had}}$ SR, except that the two $\tau_{\text{had-vis}}$ candidates have the same charge and the $E_{\mathrm{T}}^{\mathrm{miss}}$ requirement is loosened to 80 GeV. The FF is defined as the ratio of events where both $\tau_{\text{had-vis}}$ are loose to the number of events where one $\tau_{\text{had-vis}}$ is loose and the other is an anti-$\tau_{\text{had-vis}}$. These FFs are derived as a function of transverse momentum and the number of charged-particle tracks of the $\tau_{\text{had-vis}}$ candidate. The FFs are measured from data after subtracting all predicted non-multi-jet background contributions. The FFs range between approximately zero and 0.25.

The non-multi-jet background contributions that are subtracted, however, suffer from the same mismodelling issues described in the previous two sections. The top backgrounds are therefore corrected by the RFs and SFs derived as described in Section 6.1.1 and Section 6.1.2, respectively. Since the SFs are anticipated to be different for $\tau_{\text{had-vis}}$ and anti-$\tau_{\text{had-vis}}$, dedicated SFs are measured for this data-driven estimation. Specifically, the anti-$\tau_{\text{had-vis}}$ region uses SFs that are derived in a CR as described in Section 6.1.2, except that the $\tau_{\text{had-vis}}$ identification requirement is changed to that of an anti-$\tau_{\text{had-vis}}$. An example fit in a single bin of p_{T} is shown in Figure 5 for the anti-$\tau_{\text{had-vis}}$ CR. Depending on $\tau_{\text{had-vis}}$ p_{T}, these SFs vary between 0.77 and 0.95.

To construct the background estimate, FFs are applied to a region with the $\tau_{\mathrm{had}}\tau_{\mathrm{had}}$ SR selection, except that the $\tau_{\text{had-vis}}$ identification requirement is changed to that of an anti-$\tau_{\text{had-vis}}$. This provides both a shape and a normalisation for the multi-jet contribution in the PNN score distribution.

For the estimation of multi-jet backgrounds in $\tau_{\mathrm{had}}\tau_{\mathrm{had}}$, uncertainties are considered due to the statistical uncertainty of the SFs, and to the uncertainty in the subtraction of different backgrounds using simulation. Top events with a correctly identified $\tau_{\text{had-vis}}$, top events with a misidentified $\tau_{\text{had-vis}}$, and other small backgrounds are considered separately. The top events are varied by the overall uncertainty defined by the procedure to determine the modelling uncertainties, but evaluated in the anti-$\tau_{\text{had-vis}}$ region. Other backgrounds are varied by 30%. In addition, a 20% overall uncertainty in the estimate is applied based on checks of the method in validation regions. The total uncertainty in the multi-jet background is −64% to +61%.

6.3 Z + HF background

The normalisation of the Z + HF background, which is a relatively small contribution in the SRs, is observed to be in disagreement with the NLO cross-section in Sherpa (e.g. Ref. [115]). It is therefore determined from data using a Z + HF CR that targets events containing a Z boson decaying into a light-lepton pair and produced in association with two heavy-flavour jets. The composition of this control region is approximately 60% Z + HF events and 40% $t\bar{t}$ events, with less than 1% arising from backgrounds with misidentified $\tau_{\text{had-vis}}$. Since the contribution from backgrounds with misidentified $\tau_{\text{had-vis}}$ is negligible, only the RF for the $t\bar{t}$ shape is included in this CR.

Data for the CR was recorded using a combination of the single-lepton triggers described above and additional dilepton triggers requiring pairs of same-flavour leptons. At the analysis level exactly two oppositely-charged same-flavour leptons, passing the 'veto' quality requirements and p_{T} thresholds based on the corresponding trigger thresholds, are required. The invariant mass of the resulting lepton pair $m_{\ell\ell}$ is required to lie between 75 GeV and 110 GeV. In addition, exactly two b-jets with $p_{\mathrm{T}} > 20$ GeV are required and their invariant mass m_{bb} is required to be less than 40 GeV or greater than 150 GeV to avoid the Higgs boson mass peak. The RFs for top backgrounds derived in Section 6.1.1 are then applied.

A fit to the $m_{\ell\ell}$ distribution is performed to discriminate between the Z + HF and top backgrounds, with the normalisation of both processes allowed to vary freely and all systematic uncertainties described in Section 7 included. The resulting Z + HF normalisation factor is 1.36 ± 0.11 and is used to correct the Z + HF background entering into the final fit (described in Section 8), which is allowed to vary within the associated uncertainty.

7 Systematic uncertainties

The systematic uncertainties considered include detector-related uncertainties, modelling and theoretical uncertainties, and uncertainties derived for the data-driven background estimates, the latter of which have already been described in Section 6. Uncertainties are evaluated by shifting the central value upward or downward by one standard deviation, and then propagating the differences to the PNN score distributions that are used in the final fit.

Detector-related uncertainties are defined as uncertainties relating to the detector response, object reconstruction and object identification. There are systematic uncertainties associated with each of the reconstructed objects considered, as well as the $E_{\mathrm{T}}^{\mathrm{miss}}$. For light leptons, $\tau_{\text{had-vis}}$, and jets, uncertainties are considered for energy scale and resolution, reconstruction and identification, while uncertainties in isolation are also considered for light leptons. For the $\tau_{\mathrm{lep}}\tau_{\mathrm{had}}$ and $\tau_{\mathrm{had}}\tau_{\mathrm{had}}$ channel, uncertainties associated with the lepton and $\tau_{\text{had-vis}}$ trigger efficiencies, respectively, are considered. For b-jets, additional uncertainties are considered for the efficiency of (mis)tagging b-jets, c-jets, and light-quark-initiated jets. Uncertainties related to energy scale and resolution, and the inclusion of soft terms, are considered for the $E_{\mathrm{T}}^{\mathrm{miss}}$. Finally, there is also an uncertainty associated with shape and normalisation components that arises from uncertainties in the simulation of pile-up collisions.

Theoretical and modelling uncertainties include uncertainties in the cross-section calculations of background processes, which have only a normalisation component, and uncertainties in the acceptance of each process, for which normalisation and shape components are taken into account. For top backgrounds, relative acceptance uncertainties are also defined to take into account normalisation differences for $\tau_{\mathrm{lep}}\tau_{\mathrm{had}}$ and $\tau_{\mathrm{had}}\tau_{\mathrm{had}}$ SRs.

For $t\bar{t}$ processes, shape and normalisation uncertainties are considered that arise from changing the matrix element and parton shower simulation software, and from varying the initial and final state radiation, PDF, and α_s. The matrix element uncertainty is determined by comparing the Powheg+Pythia 8 sample with an aMC@NLO+Pythia 8 sample. The parton shower uncertainty is determined by comparing the Powheg+Pythia 8 sample with a Powheg+Herwig 7 [116, 117] sample. The other modelling uncertainties are evaluated using internal weights in the nominal $t\bar{t}$ sample.

For single-top processes, acceptance uncertainties with shape and normalisation components are considered. Uncertainties are considered from changing the matrix element, parton shower, and impacts

of diagram interference. In addition, variations of initial- and final-state radiation and PDFs are considered. The matrix element uncertainty is determined by comparing the POWHEG+PYTHIA 8 sample with an aMC@NLO+PYTHIA 8 sample. The parton shower uncertainty is determined by comparing the POWHEG+PYTHIA 8 sample with a POWHEG+HERWIG 7 sample. The diagram interference uncertainty is evaluated by comparing the nominal single top samples, which use a diagram removal scheme, with alternative samples that utilise a diagram subtraction scheme [118]. The other modelling uncertainties are evaluated using internal weights in the nominal single-top samples.

All $t\bar{t}$ and single-top modelling uncertainties are also propagated through the top reweighting procedure, such that there is an uncertainty in the RF corresponding to each modelling uncertainty.

For Z+jets processes, uncertainties due to the choice of generator are evaluated by comparing the nominal SHERPA simulated samples with alternative samples simulated by MADGRAPH with LO-accurate matrix elements that contain up to four final-state partons, using PYTHIA for parton showering. In addition, uncertainties are considered by taking an envelope of variations in the renormalisation and factorisation scales and PDF values using internal weights in the simulated SHERPA sample. For this process specifically, uncertainties are also included based on varying the matrix element matching scale and the resummation scale for soft-gluon emission. All of these uncertainties are included in the Z + HF fit described in Section 6.3, and their sum in quadrature, taking relative acceptance uncertainties into account, is considered as the uncertainty in the SRs for the final fit.

For signal samples, uncertainties arising from variations of scale, initial-state radiation, PDF, and α_s are considered, using alternative weights internal to the signal samples. Differences in shape are observed to be negligibly small in the PNN score distributions, so only variations in normalisation are included for the final fit.

The relative impact of the different sources of uncertainty on the analysis varies depending on the LQ model considered and the mass probed. Generally, the largest impact comes from the statistical uncertainties, which increase with m_{LQ}. In the scalar LQ case, for example, the statistical impact on the limit ranges from 60% at the lowest m_{LQ} evaluated to 80% above 1000 GeV. The main systematic uncertainties come from the $t\bar{t}$ and single-top-quark modelling uncertainties, including their interference, and normalisation. There is also a significant effect from the signal acceptance uncertainties, which increases with m_{LQ}, particularly for the vector LQ models.

8 Statistical interpretation and results

The data are compared with the expectation, including the background modelling corrections outlined in Section 6, by performing simultaneous binned maximum-likelihood fits to the PNN score distributions, separately for each LQ hypothesis, in the $\tau_{\mathrm{lep}}\tau_{\mathrm{had}}$ and $\tau_{\mathrm{had}}\tau_{\mathrm{had}}$ SRs. For each hypothesis, the binning of the PNN score distributions is chosen separately to maximise the expected sensitivity, while ensuring sufficient background events in the signal-enhanced PNN bins and preserving the stability of the fit. In addition to the relative signal-strength modifier, μ, the top normalisation is free to float in the fit and is constrained by the background-enhanced PNN bins.

The statistical and systematic uncertainties affecting the signal and background model, described in Section 7, are represented by deviations from the nominal model scaled by Gaussian- or Poisson-constrained nuisance parameters that are profiled in the fit. Common sources of systematic uncertainty are correlated across the SRs.

The resulting event yields in the $\tau_{\text{lep}}\tau_{\text{had}}$ and $\tau_{\text{had}}\tau_{\text{had}}$ SRs, based on a background-only fit to the data, are presented in Table 4. Corresponding post-fit PNN score distributions for representative LQ signals at masses of 500 GeV, 1.1 TeV and 1.4 TeV are shown in Figure 6 (Figure 7) for the $\tau_{\text{lep}}\tau_{\text{had}}$ ($\tau_{\text{had}}\tau_{\text{had}}$) SR. At high values of the PNN score, top backgrounds dominate in the $\tau_{\text{lep}}\tau_{\text{had}}$ channel, while the $\tau_{\text{had}}\tau_{\text{had}}$ background consists of a roughly even mixture of all background sources. Overall, good agreement with the SM background expectation is observed in all cases, although there is a slight deficit of data relative to the background prediction in the highest PNN score bin for the $\tau_{\text{had}}\tau_{\text{had}}$ channel.

Table 4: Post-fit yields for background events, determined from a background-only fit, compared with the observed number of data events in the $\tau_{\text{lep}}\tau_{\text{had}}$ and $\tau_{\text{had}}\tau_{\text{had}}$ SRs. 'Fake τ_{had} (top)' refers to top backgrounds where a jet is misidentified as the $\tau_{\text{had-vis}}$ of the event, and 'Other' refers to the sum of minor backgrounds (vector boson + jets, diboson and Higgs boson). The total background is not identical to the sum of the individual components since the latter are rounded for presentation, while the sum is calculated with the full precision before being subsequently rounded. Systematic uncertainties are included. Due to the large correlations, individual uncertainties can be significantly larger than the total uncertainty.

	$\tau_{\text{lep}}\tau_{\text{had}}$ channel	$\tau_{\text{had}}\tau_{\text{had}}$ channel
$t\bar{t}$	2420 ± 90	93 ± 9
single-top	355 ± 27	20 ± 4
Fake τ_{had} (top)	170 ± 90	43 ± 18
$Z\rightarrow\tau\tau$ + (bb, bc, cc)	13.9 ± 2.4	10.3 ± 1.4
Multi-jet	–	22 ± 11
Other	78 ± 7	19 ± 5
Total Background	3040 ± 60	207 ± 13
Data	3031	211

Since no significant excess is observed, upper limits on the scalar and vector LQ pair production cross-sections for each mass hypothesis are computed based on the modified frequentist CL_s method [119], using a profile likelihood test statistic [120] under the asymptotic approximation. The resulting observed and expected limits, assuming $\mathcal{B} = 1$, as a function of m_{LQ} at 95% confidence level (CL) are shown in Figure 8 for all LQ models. The expected contributions of the $\tau_{\text{lep}}\tau_{\text{had}}$ and $\tau_{\text{had}}\tau_{\text{had}}$ channels are approximately equal at high m_{LQ}, while the $\tau_{\text{had}}\tau_{\text{had}}$ is up to a factor of two more sensitive at low m_{LQ}. The improvement in the observed limit compared with the expectation is driven by the data deficit in the highest $\tau_{\text{had}}\tau_{\text{had}}$ PNN score bin mentioned above and is larger at high m_{LQ} since the signal becomes more localised at high PNN score as m_{LQ} increases. The theoretical prediction for the cross-section of scalar or vector LQ pair production is indicated by the solid line along with its uncertainties.

Table 5: Observed and expected lower limits on the LQ mass at 95% CL for the three different LQ models, assuming $\mathcal{B} = 1$.

	Obs. limit [GeV]	Exp. limit [GeV]
Scalar LQ	1490	1410
Vector LQ (minimal-coupling)	1690	1600
Vector LQ (Yang–Mills)	1960	1840

The corresponding expected and observed 95% CL lower limits on the LQ mass for the three different

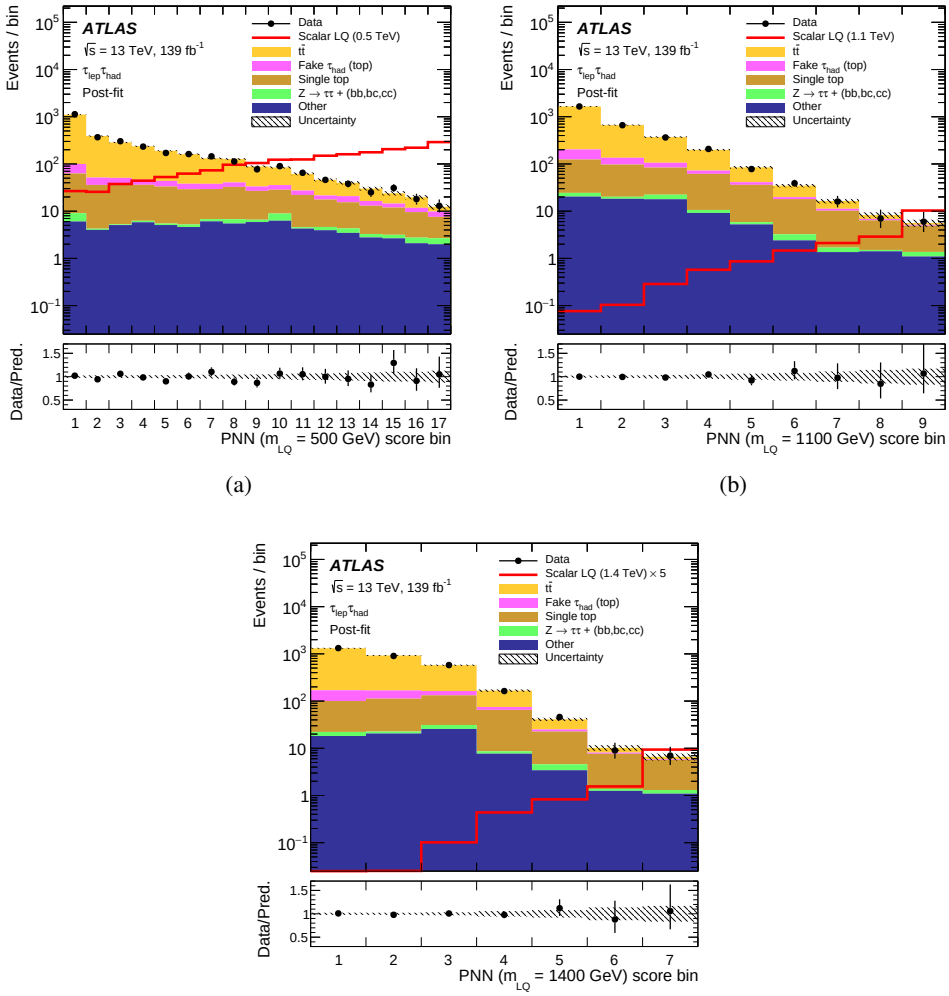

Figure 6: The PNN score distributions in the $\tau_{\text{lep}}\tau_{\text{had}}$ SR for (a) $m_{\text{LQ}} = 500\,\text{GeV}$, (b) $m_{\text{LQ}} = 1.1\,\text{TeV}$, (c) $m_{\text{LQ}} = 1.4\,\text{TeV}$. The normalisation and shape of the backgrounds are determined from the background-only likelihood fit to data and the ratios of the data to the sum of the backgrounds are shown in the lower panels. 'Other' refers to the sum of minor backgrounds (vector boson + jets, diboson and Higgs boson). The hatched bands indicate the combined statistical and systematic uncertainty in the total background predictions. The expected signals for scalar LQs with the corresponding masses, scaled by the indicated factors for visibility, are overlaid. Since the PNN score itself is not a physical quantity, it is represented solely by the bin number.

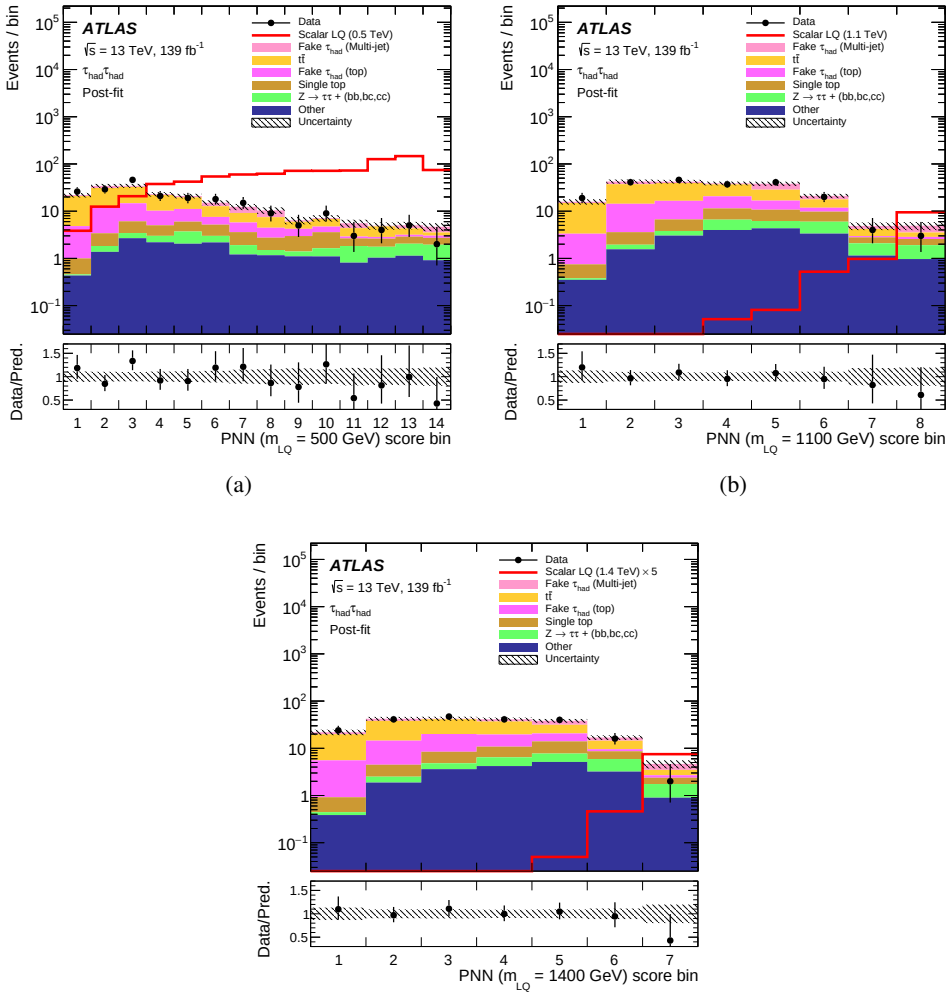

Figure 7: The PNN score distributions in the $\tau_{\text{had}}\tau_{\text{had}}$ SR for (a) $m_{\text{LQ}} = 500\,\text{GeV}$, (b) $m_{\text{LQ}} = 1.1\,\text{TeV}$, (c) $m_{\text{LQ}} = 1.4\,\text{TeV}$. The normalisation and shape of the backgrounds are determined from the background-only likelihood fit to data and the ratios of the data to the sum of the backgrounds are shown in the lower panels. 'Other' refers to the sum of minor backgrounds (vector boson + jets, diboson and Higgs boson). The hatched bands indicate the combined statistical and systematic uncertainty in the total background predictions. The expected signals for scalar LQs with the corresponding masses, scaled by the indicated factors for visibility, are overlaid. Since the PNN score itself is not a physical quantity, it is represented solely by the bin number.

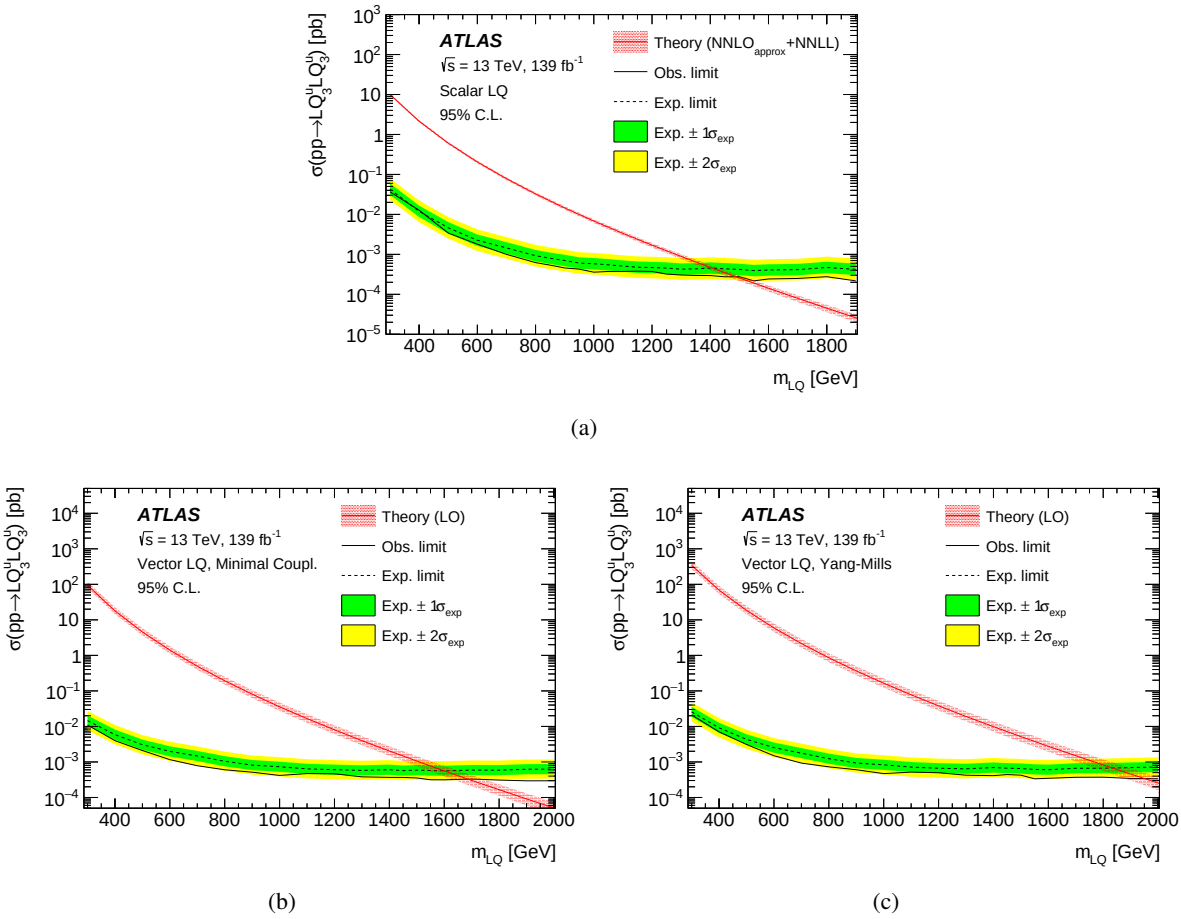

Figure 8: The observed (solid line) and expected (dashed line) 95% CL upper limits on the LQ pair production cross-sections assuming $\mathcal{B} = 1$ as a function of m_{LQ} for (a) the scalar LQ case, (b) the vector LQ case in the minimal-coupling scenario, (c) vector LQs in the Yang–Mills scenario. The surrounding shaded bands correspond to the ± 1 and ± 2 standard deviation ($\pm 1\sigma, \pm 2\sigma$) uncertainty in the expected limit. The theoretical prediction in each model, along with its uncertainty, is shown by the lines with the hatched bands.

LQ models are summarised in Table 5, providing an improvement in mass reach for a scalar LQ of more than 450 GeV compared with the previous 36 fb^{-1} result in this channel [18]. They extend the full Run 2 ATLAS reach for third-generation up-type LQs by around 200 GeV in all three models compared with the search in the $LQLQ \to t\nu t\nu$ decay mode [26].

The results are also expressed as upper limits on the branching ratio to charged leptons as a function of m_{LQ} for each LQ model in Figure 9. For all models investigated, constraints on the LQ mass are reduced by no more than 15% going from $\mathcal{B} = 1$ to $\mathcal{B} = 0.5$, while scalar LQ masses up to around 850 GeV are excluded for couplings into charged leptons as low as 0.1; the corresponding $\mathcal{B} = 0.1$ exclusion for vector LQ is around 1100 GeV (1300 GeV) in the minimal-coupling (Yang–Mills) scenario.

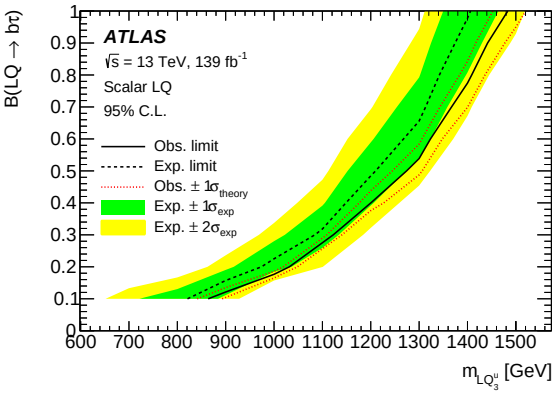

(a)

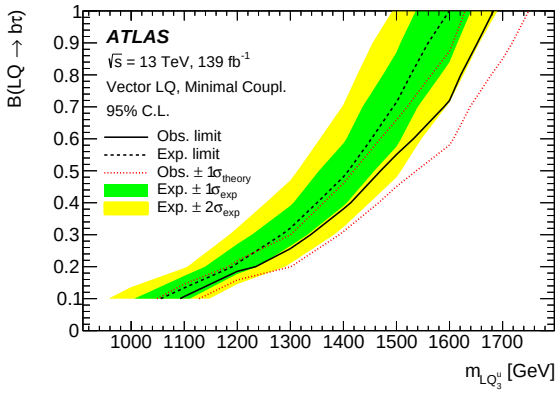

(b)

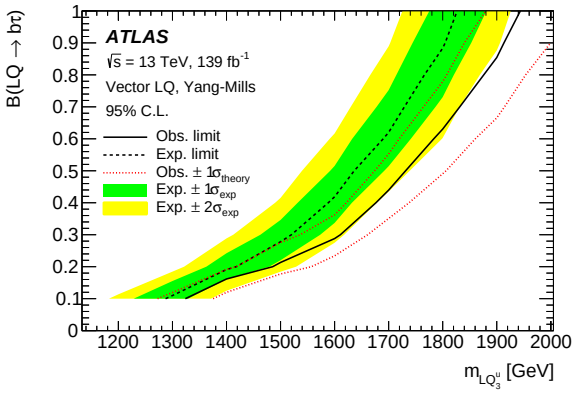

(c)

Figure 9: The observed (solid line) and expected (dashed line) 95% CL upper limits on the branching ratio into charged leptons as a function of m_{LQ} for (a) the scalar LQ case, (b) the vector LQ case in the minimal-coupling scenario, (c) vector LQs in the Yang–Mills scenario. The observed exclusion region is above the solid line, with the theoretical uncertainty in the model indicated by the dotted lines around this. The expected limit is indicated by the dashed line and the surrounding shaded bands correspond to the ±1 and ±2 standard deviation ($\pm 1\sigma, \pm 2\sigma$) uncertainty in the expected limit. No limits are presented for $\mathcal{B} < 0.1$ due to the lack of expected signal events in this final state.

9 Conclusion

A search for pair-produced scalar or vector leptoquarks decaying into a b-quark and a τ-lepton is presented. The analysis exploits the full data sample recorded with the ATLAS detector in Run 2 of the LHC, corresponding to 139 fb^{-1} of proton–proton collisions at $\sqrt{s} = 13$ TeV. No significant deviations from the Standard Model expectation are observed and upper limits on the production cross-section are derived as a function of LQ mass and branching ratio into a charged lepton. Scalar LQs with masses below 1490 GeV are excluded assuming a 100% branching ratio, while for vector LQs the corresponding limit is 1690 GeV (1960 GeV) in the minimal-coupling (Yang–Mills) scenario. For branching ratios as low as 10%, scalar LQ masses below around 850 GeV are excluded; the corresponding mass limits for vector LQs are 1100 GeV (1300 GeV) in the minimal-coupling (Yang–Mills) scenario. These results significantly improve the sensitivity compared to previous ATLAS LQ searches, extending the mass reach for third-generation up-type LQs by more than 200 GeV in all models and surpassing the previous ATLAS search in this final state by more than 450 GeV for scalar LQs. In addition to the increased luminosity, this is due to upgraded hadronic τ-lepton and b-jet identification, improved multivariate techniques and better background estimation methods.

References

[1] J. C. Pati and A. Salam, *Lepton number as the fourth "color"*, Phys. Rev. D **10** (1 1974) 275.

[2] H. Georgi and S. L. Glashow, *Unity of All Elementary-Particle Forces*, Phys. Rev. Lett. **32** (8 1974) 438.

[3] S. Dimopoulos and L. Susskind, *Mass without scalars*, Nuclear Physics B **155** (1979) 237.

[4] S. Dimopoulos, *Technicoloured signatures*, Nuclear Physics B **168** (1980) 69.

[5] E. Eichten and K. Lane, *Dynamical breaking of weak interaction symmetries*, Physics Letters B **90** (1980) 125.

[6] V. D. Angelopoulos et al., *Search for new quarks suggested by the superstring*, Nuclear Physics B **292** (1987) 59.

[7] W. Buchmüller and D. Wyler, *Constraints on SU(5)-type leptoquarks*, Physics Letters B **177** (1986) 377.

[8] G. Hiller and M. Schmaltz, *R_K and future $b \to s\ell\ell$ physics beyond the standard model opportunities*, Phys. Rev. D **90** (2014) 054014, arXiv: 1408.1627 [hep-ph].

[9] B. Gripaios, M. Nardecchia and S. A. Renner, *Composite leptoquarks and anomalies in B-meson decays*, JHEP **05** (2015) 006, arXiv: 1412.1791 [hep-ph].

[10] M. Freytsis, Z. Ligeti and J. T. Ruderman, *Flavor models for $\bar{B} \to D^{(*)}\tau\bar{\nu}$*, Phys. Rev. D **92** (2015) 054018, arXiv: 1506.08896 [hep-ph].

[11] M. Bauer and M. Neubert, *Minimal Leptoquark Explanation for the $R_{D^{(*)}}$, R_K , and $(g-2)_\mu$ Anomalies*, Phys. Rev. Lett. **116** (2016) 141802, arXiv: 1511.01900 [hep-ph].

[12] L. Di Luzio and M. Nardecchia, *What is the scale of new physics behind the B-flavour anomalies?*, Eur. Phys. J. C **77** (2017) 536, arXiv: 1706.01868 [hep-ph].

[13] D. Buttazzo, A. Greljo, G. Isidori and D. Marzocca, *B-physics anomalies: a guide to combined explanations*, JHEP **11** (2017) 044, arXiv: 1706.07808 [hep-ph].

[14] R. Aaij et al., *Test of Lepton Universality Using $B^+ \to K^+\ell^+\ell^-$ Decays*, Phys. Rev. Lett. **113** (2014) 151601, arXiv: 1406.6482 [hep-ex].

[15] W. Buchmüller, R. Rückl and D. Wyler, *Leptoquarks in lepton-quark collisions*, Physics Letters B **191** (1987) 442.

[16] M. J. Baker, J. Fuentes-Martín, G. Isidori and M. König, *High-p_T signatures in vector–leptoquark models*, Eur. Phys. J. C **79** (2019) 334, arXiv: 1901.10480 [hep-ph].

[17] ATLAS Collaboration, *Search for pair production of scalar leptoquarks decaying into first- or second-generation leptons and top quarks in proton–proton collisions at $\sqrt{s} = 13$ TeV with the ATLAS detector*, Eur. Phys. J. C **81** (2021) 313, arXiv: 2010.02098 [hep-ex].

[18] ATLAS Collaboration, *Searches for third-generation scalar leptoquarks in $\sqrt{s} = 13$ TeV pp collisions with the ATLAS detector*, JHEP **06** (2019) 144, arXiv: 1902.08103 [hep-ex].

[19] ATLAS Collaboration, *Search for pair production of third-generation scalar leptoquarks decaying into a top quark and a τ-lepton in pp collisions at $\sqrt{s} = 13$ TeV with the ATLAS detector*, JHEP **06** (2021) 179, arXiv: 2101.11582 [hep-ex].

[20] ATLAS Collaboration, *Search for a scalar partner of the top quark in the all-hadronic $t\bar{t}$ plus missing transverse momentum final state at $\sqrt{s} = 13$ TeV with the ATLAS detector*, Eur. Phys. J. C **80** (2020) 737, arXiv: 2004.14060 [hep-ex].

[21] ATLAS Collaboration, *Search for new phenomena in final states with b-jets and missing transverse momentum in $\sqrt{s} = 13$ TeV pp collisions with the ATLAS detector*, JHEP **05** (2021) 093, arXiv: 2101.12527 [hep-ex].

[22] CMS Collaboration, *Search for singly and pair-produced leptoquarks coupling to third-generation fermions in proton–proton collisions at $\sqrt{s} = 13$ TeV*, Phys. Lett. B **819** (2020) 136446, arXiv: 2012.04178 [hep-ex].

[23] CMS Collaboration, *Search for pair production of first-generation scalar leptoquarks at $\sqrt{s} = 13$ TeV*, Phys. Rev. D **99** (2019) 052002, arXiv: 1811.01197 [hep-ex].

[24] CMS Collaboration, *Search for heavy neutrinos and third-generation leptoquarks in hadronic states of two τ leptons and two jets in proton–proton collisions at $\sqrt{s} = 13$ TeV*, JHEP **03** (2019) 170, arXiv: 1811.00806 [hep-ex].

[25] CMS Collaboration, *Search for pair production of second-generation leptoquarks at $\sqrt{s} = 13$ TeV*, Phys. Rev. D **99** (2019) 032014, arXiv: 1808.05082 [hep-ex].

[26] ATLAS Collaboration, *Search for new phenomena in pp collisions in final states with tau leptons, b-jets, and missing transverse momentum with the ATLAS detector*, Phys. Rev. D **104** (2021) 112005, arXiv: 2108.07665 [hep-ex].

[27] B. Diaz, M. Schmaltz and Y.-M. Zhong, *The leptoquark hunter's guide: pair production*, JHEP **10** (2017) 097, arXiv: 1706.05033 [hep-ph].

[28] ATLAS Collaboration, *The ATLAS Experiment at the CERN Large Hadron Collider*, JINST **3** (2008) S08003.

[29] ATLAS Collaboration, *ATLAS Insertable B-Layer: Technical Design Report*, ATLAS-TDR-19; CERN-LHCC-2010-013, 2010, URL: https://cds.cern.ch/record/1291633, Addendum: ATLAS-TDR-19-ADD-1; CERN-LHCC-2012-009, 2012, URL: https://cds.cern.ch/record/1451888.

[30] B. Abbott et al., *Production and integration of the ATLAS Insertable B-Layer*, JINST **13** (2018) T05008, arXiv: 1803.00844 [physics.ins-det].

[31] ATLAS Collaboration, *Performance of the ATLAS trigger system in 2015*, Eur. Phys. J. C **77** (2017) 317, arXiv: 1611.09661 [hep-ex].

[32] ATLAS Collaboration, *The ATLAS Collaboration Software and Firmware*, ATL-SOFT-PUB-2021-001, 2021, URL: https://cds.cern.ch/record/2767187.

[33] ATLAS Collaboration, *Luminosity determination in pp collisions at $\sqrt{s} = 13$ TeV using the ATLAS detector at the LHC*, ATLAS-CONF-2019-021, 2019, URL: https://cds.cern.ch/record/2677054.

[34] G. Avoni et al., *The new LUCID-2 detector for luminosity measurement and monitoring in ATLAS*, JINST **13** (2018) P07017.

[35] ATLAS Collaboration, *The ATLAS Simulation Infrastructure*, Eur. Phys. J. C **70** (2010) 823, arXiv: 1005.4568 [physics.ins-det].

[36] GEANT4 Collaboration, S. Agostinelli et al., *GEANT4 – a simulation toolkit*, Nucl. Instrum. Meth. A **506** (2003) 250.

[37] ATLAS Collaboration, *The simulation principle and performance of the ATLAS fast calorimeter simulation FastCaloSim*, ATL-PHYS-PUB-2010-013, 2010, URL: https://cds.cern.ch/record/1300517.

[38] T. Sjöstrand, S. Mrenna and P. Skands, *A brief introduction to PYTHIA 8.1*, Comput. Phys. Commun. **178** (2008) 852, arXiv: 0710.3820 [hep-ph].

[39] R. D. Ball et al., *Parton distributions with LHC data*, Nucl. Phys. B **867** (2013) 244, arXiv: 1207.1303 [hep-ph].

[40] ATLAS Collaboration, *The Pythia 8 A3 tune description of ATLAS minimum bias and inelastic measurements incorporating the Donnachie–Landshoff diffractive model*, ATL-PHYS-PUB-2016-017, 2016, URL: https://cds.cern.ch/record/2206965.

[41] J. Alwall et al., *The automated computation of tree-level and next-to-leading order differential cross sections, and their matching to parton shower simulations*, JHEP **07** (2014) 079, arXiv: 1405.0301 [hep-ph].

[42] T. Mandal, S. Mitra and S. Seth, *Pair Production of scalar leptoquarks at the LHC to NLO parton shower accuracy*, Phys. Rev. D **93** (2016) 035018, arXiv: 1506.07369 [hep-ph].

[43] M. Kramer, T. Plehn, M. Spira and P. M. Zerwas, *Pair production of scalar leptoquarks at the CERN LHC*, Phys. Rev. D **71** (2005) 057503, arXiv: hep-ph/0411038.

[44] M. Kramer, T. Plehn, M. Spira and P. M. Zerwas,
Pair Production of Scalar Leptoquarks at the Fermilab Tevatron, Phys. Rev. Lett. **79** (1997) 341, arXiv: hep-ph/9704322.

[45] T. Sjöstrand et al., *An introduction to PYTHIA 8.2*, Comput. Phys. Commun. **191** (2015) 159, arXiv: 1410.3012 [hep-ph].

[46] R. D. Ball et al., *Parton distributions for the LHC run II*, JHEP **04** (2015) 040, arXiv: 1410.8849 [hep-ph].

[47] ATLAS Collaboration, *ATLAS Pythia 8 tunes to 7 TeV data*, ATL-PHYS-PUB-2014-021, 2014, URL: https://cds.cern.ch/record/1966419.

[48] ATLAS Collaboration, *Summary of ATLAS Pythia 8 tunes*, ATL-PHYS-PUB-2012-003, 2012, URL: https://cds.cern.ch/record/1474107.

[49] P. Artoisenet, R. Frederix, O. Mattelaer and R. Rietkerk,
Automatic spin-entangled decays of heavy resonances in Monte Carlo simulations, JHEP **03** (2013) 015, arXiv: 1212.3460 [hep-ph].

[50] W. Beenakker, C. Borschensky, M. Krämer, A. Kulesza and E. Laenen,
NNLL-fast: predictions for coloured supersymmetric particle production at the LHC with threshold and Coulomb resummation, JHEP **12** (2016) 133, arXiv: 1607.07741 [hep-ph].

[51] W. Beenakker, M. Kramer, T. Plehn, M. Spira and P. M. Zerwas,
Stop production at hadron colliders, Nucl. Phys. B **515** (1998) 3, arXiv: hep-ph/9710451.

[52] W. Beenakker et al., *Supersymmetric top and bottom squark production at hadron colliders*, JHEP **08** (2010) 098, arXiv: 1006.4771 [hep-ph].

[53] W. Beenakker et al., *NNLL resummation for stop pair-production at the LHC*, JHEP **05** (2016) 153, arXiv: 1601.02954 [hep-ph].

[54] C. Borschensky, B. Fuks, A. Kulesza and D. Schwartländer,
Scalar leptoquark pair production at hadron colliders, Phys. Rev. D **101** (2020) 115017, arXiv: 2002.08971 [hep-ph].

[55] J. Butterworth et al., *PDF4LHC recommendations for LHC Run II*, J. Phys. G **43** (2016) 023001, arXiv: 1510.03865 [hep-ph].

[56] M. L. Ciccolini, S. Dittmaier and M. Krämer,
Electroweak radiative corrections to associated WH and ZH production at hadron colliders, Phys. Rev. D **68** (2003) 073003, arXiv: hep-ph/0306234 [hep-ph].

[57] O. Brein, A. Djouadi and R. Harlander,
NNLO QCD corrections to the Higgs-strahlung processes at hadron colliders, Phys. Lett. B **579** (2004) 149, arXiv: hep-ph/0307206.

[58] G. Ferrera, M. Grazzini and F. Tramontano, *Associated Higgs-W-Boson Production at Hadron Colliders: A Fully Exclusive QCD Calculation at NNLO*, Phys. Rev. Lett. **107** (2011) 152003, arXiv: 1107.1164 [hep-ph].

[59] O. Brein, R. V. Harlander, M. Wiesemann and T. Zirke,
Top-quark mediated effects in hadronic Higgs-Strahlung, Eur. Phys. J. C **72** (2012) 1868, arXiv: 1111.0761 [hep-ph].

[60] G. Ferrera, M. Grazzini and F. Tramontano,
Associated ZH production at hadron colliders: The fully differential NNLO QCD calculation,
Phys. Lett. B **740** (2015) 51, arXiv: 1407.4747 [hep-ph].

[61] J. M. Campbell, R. K. Ellis and C. Williams, *Associated production of a Higgs boson at NNLO*,
JHEP **06** (2016) 179, arXiv: 1601.00658 [hep-ph].

[62] S. Alioli, P. Nason, C. Oleari and E. Re, *A general framework for implementing NLO calculations in shower Monte Carlo programs: the POWHEG BOX*, JHEP **06** (2010) 043,
arXiv: 1002.2581 [hep-ph].

[63] M. Czakon and A. Mitov,
Top++: A program for the calculation of the top-pair cross-section at hadron colliders,
Comput. Phys. Commun. **185** (2014) 2930, arXiv: 1112.5675 [hep-ph].

[64] N. Kidonakis,
Next-to-next-to-leading logarithm resummation for s-channel single top quark production,
Phys. Rev. D **81** (2010) 054028, arXiv: 1001.5034 [hep-ph].

[65] N. Kidonakis, *Next-to-next-to-leading-order collinear and soft gluon corrections for t-channel single top quark production*, Phys. Rev. D **83** (2011) 091503, arXiv: 1103.2792 [hep-ph].

[66] N. Kidonakis,
Two-loop soft anomalous dimensions for single top quark associated production with a W^- or H^-,
Phys. Rev. D **82** (2010) 054018, arXiv: 1005.4451 [hep-ph].

[67] E. Bothmann et al., *Event Generation with Sherpa 2.2*, SciPost Phys. **7** (2019) 034,
arXiv: 1905.09127 [hep-ph].

[68] T. Gleisberg and S. Höche, *Comix, a new matrix element generator*, JHEP **12** (2008) 039,
arXiv: 0808.3674 [hep-ph].

[69] F. Cascioli, P. Maierhöfer and S. Pozzorini, *Scattering Amplitudes with Open Loops*,
Phys. Rev. Lett. **108** (2012) 111601, arXiv: 1111.5206 [hep-ph].

[70] S. Catani, L. Cieri, G. Ferrera, D. de Florian and M. Grazzini, *Vector Boson Production at Hadron Colliders: A Fully Exclusive QCD Calculation at Next-to-Next-to-Leading Order*,
Phys. Rev. Lett. **103** (2009) 082001, arXiv: 0903.2120 [hep-ph].

[71] ATLAS Collaboration, *Measurement of the Z/γ^* boson transverse momentum distribution in pp collisions at $\sqrt{s} = 7$ TeV with the ATLAS detector*, JHEP **09** (2014) 145,
arXiv: 1406.3660 [hep-ex].

[72] D. de Florian et al.,
Handbook of LHC Higgs Cross Sections: 4. Deciphering the Nature of the Higgs Sector, (2016),
arXiv: 1610.07922 [hep-ph].

[73] C. Anastasiou et al.,
High precision determination of the gluon fusion Higgs boson cross-section at the LHC,
JHEP **05** (2016) 058, arXiv: 1602.00695 [hep-ph].

[74] C. Anastasiou, C. Duhr, F. Dulat, F. Herzog and B. Mistlberger,
Higgs Boson Gluon-Fusion Production in QCD at Three Loops,
Phys. Rev. Lett. **114** (2015) 212001, arXiv: 1503.06056 [hep-ph].

[75] F. Dulat, A. Lazopoulos and B. Mistlberger, *iHixs 2 – Inclusive Higgs cross sections*,
Comput. Phys. Commun. **233** (2018) 243, arXiv: 1802.00827 [hep-ph].

[76] S. Actis, G. Passarino, C. Sturm and S. Uccirati,
NLO electroweak corrections to Higgs boson production at hadron colliders,
Phys. Lett. B **670** (2008) 12, arXiv: 0809.1301 [hep-ph].

[77] M. Ciccolini, A. Denner and S. Dittmaier, *Strong and Electroweak Corrections to the Production of a Higgs Boson + 2 Jets via Weak Interactions at the Large Hadron Collider*,
Phys. Rev. Lett. **99** (2007) 161803, arXiv: 0707.0381 [hep-ph].

[78] M. Ciccolini, A. Denner and S. Dittmaier,
Electroweak and QCD corrections to Higgs production via vector-boson fusion at the CERN LHC,
Phys. Rev. D **77** (2008) 013002, arXiv: 0710.4749 [hep-ph].

[79] P. Bolzoni, F. Maltoni, S.-O. Moch and M. Zaro,
Higgs Boson Production via Vector-Boson Fusion at Next-to-Next-to-Leading Order in QCD,
Phys. Rev. Lett. **105** (2010) 011801, arXiv: 1003.4451 [hep-ph].

[80] G. Ferrera, M. Grazzini and F. Tramontano,
Higher-order QCD effects for associated WH production and decay at the LHC,
JHEP **04** (2014) 039, arXiv: 1312.1669 [hep-ph].

[81] L. Altenkamp, S. Dittmaier, R. V. Harlander, H. Rzehak and T. J. E. Zirke,
Gluon-induced Higgs-strahlung at next-to-leading order QCD, JHEP **02** (2013) 078,
arXiv: 1211.5015 [hep-ph].

[82] B. Hespel, F. Maltoni and E. Vryonidou,
Higgs and Z boson associated production via gluon fusion in the SM and the 2HDM,
JHEP **06** (2015) 065, arXiv: 1503.01656 [hep-ph].

[83] R. V. Harlander, A. Kulesza, V. Theeuwes and T. Zirke,
Soft gluon resummation for gluon-induced Higgs Strahlung, JHEP **11** (2014) 082,
arXiv: 1410.0217 [hep-ph].

[84] R. V. Harlander, S. Liebler and T. Zirke,
Higgs Strahlung at the Large Hadron Collider in the 2-Higgs-doublet model, JHEP **02** (2014) 023,
arXiv: 1307.8122 [hep-ph].

[85] O. Brein, R. V. Harlander and T. J. E. Zirke, *vh@nnlo – Higgs Strahlung at hadron colliders*,
Comput. Phys. Commun. **184** (2013) 998, arXiv: 1210.5347 [hep-ph].

[86] D. J. Lange, *The EvtGen particle decay simulation package*,
Nucl. Instrum. Meth. A **462** (2001) 152.

[87] ATLAS Collaboration, *Electron and photon performance measurements with the ATLAS detector using the 2015–2017 LHC proton–proton collision data*, JINST **14** (2019) P12006,
arXiv: 1908.00005 [hep-ex].

[88] ATLAS Collaboration, *Muon reconstruction and identification efficiency in ATLAS using the full Run 2 pp collision data set at $\sqrt{s} = 13$ TeV*, Eur. Phys. J. C **81** (2021) 578,
arXiv: 2012.00578 [hep-ex].

[89] ATLAS Collaboration, *Muon reconstruction performance of the ATLAS detector in proton–proton collision data at $\sqrt{s} = 13$ TeV*, Eur. Phys. J. C **76** (2016) 292, arXiv: 1603.05598 [hep-ex].

[90] ATLAS Collaboration,
Jet reconstruction and performance using particle flow with the ATLAS Detector,
Eur. Phys. J. C **77** (2017) 466, arXiv: 1703.10485 [hep-ex].

[91] M. Cacciari, G. P. Salam and G. Soyez, *The anti-k_t jet clustering algorithm*, JHEP **04** (2008) 063, arXiv: 0802.1189 [hep-ph].

[92] M. Cacciari, G. P. Salam and G. Soyez, *FastJet user manual*, Eur. Phys. J. C **72** (2012) 1896, arXiv: 1111.6097 [hep-ph].

[93] ATLAS Collaboration, *Performance of pile-up mitigation techniques for jets in pp collisions at $\sqrt{s} = 8$ TeV using the ATLAS detector*, Eur. Phys. J. C **76** (2016) 581, arXiv: 1510.03823 [hep-ex].

[94] ATLAS Collaboration, *ATLAS b-jet identification performance and efficiency measurement with $t\bar{t}$ events in pp collisions at $\sqrt{s} = 13$ TeV*, Eur. Phys. J. C **79** (2019) 970, arXiv: 1907.05120 [hep-ex].

[95] ATLAS Collaboration, *Optimisation and performance studies of the ATLAS b-tagging algorithms for the 2017-18 LHC run*, ATL-PHYS-PUB-2017-013, 2017, URL: https://cds.cern.ch/record/2273281.

[96] *ATLAS flavour-tagging algorithms for the LHC Run 2 pp collision dataset*, (2022), arXiv: 2211.16345 [physics.data-an], URL: https://cds.cern.ch/record/2842028.

[97] ATLAS Collaboration, *Calibration of light-flavour b-jet mistagging rates using ATLAS proton–proton collision data at $\sqrt{s} = 13$ TeV*, ATLAS-CONF-2018-006, 2018, URL: https://cds.cern.ch/record/2314418.

[98] ATLAS Collaboration, *Measurement of the c-jet mistagging efficiency in $t\bar{t}$ events using pp collision data at $\sqrt{s} = 13$ TeV collected with the ATLAS detector*, Eur. Phys. J. C **82** (2021) 95, arXiv: 2109.10627 [hep-ex].

[99] ATLAS Collaboration, *Identification and energy calibration of hadronically decaying tau leptons with the ATLAS experiment in pp collisions at $\sqrt{s} = 8$ TeV*, Eur. Phys. J. C **75** (2015) 303, arXiv: 1412.7086 [hep-ex].

[100] ATLAS Collaboration, *Identification of hadronic tau lepton decays using neural networks in the ATLAS experiment*, ATL-PHYS-PUB-2019-033, 2019, URL: https://cds.cern.ch/record/2688062.

[101] ATLAS Collaboration, *Measurement of the tau lepton reconstruction and identification performance in the ATLAS experiment using pp collisions at $\sqrt{s} = 13$ TeV*, ATLAS-CONF-2017-029, 2017, URL: https://cds.cern.ch/record/2261772.

[102] ATLAS Collaboration, *Performance of missing transverse momentum reconstruction with the ATLAS detector using proton–proton collisions at $\sqrt{s} = 13$ TeV*, Eur. Phys. J. C **78** (2018) 903, arXiv: 1802.08168 [hep-ex].

[103] ATLAS Collaboration, *E_T^{miss} performance in the ATLAS detector using 2015–2016 LHC pp collisions*, ATLAS-CONF-2018-023, 2018, URL: https://cds.cern.ch/record/2625233.

[104] ATLAS Collaboration, *Performance of electron and photon triggers in ATLAS during LHC Run 2*, Eur. Phys. J. C **80** (2020) 47, arXiv: 1909.00761 [hep-ex].

[105] ATLAS Collaboration, *Performance of the ATLAS muon triggers in Run 2*, JINST **15** (2020) P09015, arXiv: 2004.13447 [hep-ex].

[106] ATLAS Collaboration, *The ATLAS Tau Trigger in Run 2*, ATLAS-CONF-2017-061, 2017, URL: https://cds.cern.ch/record/2274201.

[107] A. Elagin, P. Murat, A. Pranko and A. Safonov,
A new mass reconstruction technique for resonances decaying to $\tau\tau$,
Nucl. Instrum. Meth. A **654** (2011) 481, arXiv: 1012.4686 [hep-ex].

[108] P. Baldi, K. Cranmer, T. Faucett, P. Sadowski and D. Whiteson,
Parameterized neural networks for high-energy physics, Eur. Phys. J. C **76** (2016) 235,
arXiv: 1601.07913 [hep-ex].

[109] F. Chollet et al., *Keras*, https://keras.io, 2015.

[110] M Abadi et al., *TensorFlow: Large-Scale Machine Learning on Heterogeneous Systems*,
Software available from tensorflow.org, 2015, URL: https://www.tensorflow.org/.

[111] ATLAS Collaboration, *A search for resonant and non-resonant Higgs boson pair production in the $b\bar{b}\tau^+\tau^-$ decay channel in pp collisions at $\sqrt{s} = 13$ TeV with the ATLAS detector*,
Phys. Rev. Lett. **121** (2018) 191801, arXiv: 1808.00336 [hep-ex],
Erratum: Phys. Rev. Lett. **122** (2019) 089901.

[112] ATLAS Collaboration, *Measurement of the $t\bar{t}$ production cross-section and lepton differential distributions in $e\mu$ dilepton events from pp collisions at $\sqrt{s} = 13$ TeV with the ATLAS detector*,
Eur. Phys. J. C **80** (2020) 528, arXiv: 1910.08819 [hep-ex].

[113] ATLAS Collaboration,
Measurements of top-quark pair single- and double-differential cross-sections in the all-hadronic channel in pp collisions at $\sqrt{s} = 13$ TeV using the ATLAS detector, JHEP **01** (2021) 033,
arXiv: 2006.09274 [hep-ex].

[114] ATLAS Collaboration, *Measurements of top-quark pair differential and double-differential cross-sections in the ℓ+jets channel with pp collisions at $\sqrt{s} = 13$ TeV using the ATLAS detector*,
Eur. Phys. J. C **79** (2019) 1028, arXiv: 1908.07305 [hep-ex],
Erratum: Eur. Phys. J. C **80** (2020) 1092.

[115] ATLAS Collaboration, *Evidence for the $H \to b\bar{b}$ decay with the ATLAS detector*,
JHEP **12** (2017) 024, arXiv: 1708.03299 [hep-ex].

[116] M. Bähr et al., *Herwig++ physics and manual*, Eur. Phys. J. C **58** (2008) 639,
arXiv: 0803.0883 [hep-ph].

[117] J. Bellm et al., *Herwig 7.0/Herwig++ 3.0 release note*, Eur. Phys. J. C **76** (2016) 196,
arXiv: 1512.01178 [hep-ph].

[118] S. Frixione, E. Laenen, P. Motylinski, C. White and B. R. Webber,
Single-top hadroproduction in association with a W boson, JHEP **07** (2008) 029,
arXiv: 0805.3067 [hep-ph].

[119] A. L. Read, *Presentation of search results: the CL_S technique*, J. Phys. G **28** (2002) 2693.

[120] G. Cowan, K. Cranmer, E. Gross and O. Vitells,
Asymptotic formulae for likelihood-based tests of new physics, Eur. Phys. J. C **71** (2011) 1554,
arXiv: 1007.1727 [physics.data-an], Erratum: Eur. Phys. J. C **73** (2013) 2501.